High-throughput single molecule tracking identifies drug interactions and cellular mechanisms

David T. McSwiggen, Helen Liu, Ruensern Tan, Sebastia Agramunt Puig, Lakshmi B. Akella, Russell Berman, Mason Bretan, Hanzhe Chen, Xavier Darzacq, Kelsey Ford, Ruth Godbey, Eric Gonzalez, Adi Hanuka, Alec Heckert, Jaclyn J. Ho, Stephanie L. Johnson, Reed Kelso, Aaron Klammer, Jifu Li, Kevin Lin, Brian Margolin, Patrick McNamara, Lawrence Meyer, Sarah E. Pierce, Akshay Sule, Yangzhong Tang, Daniel J. Anderson, Hilary P. Beck

Abstract

The regulation of cell physiology largely depends upon intracellular interactions of functionally distinct proteins that act in combination. These interactions, which are often transient in nature, help to define the motion profiles of proteins. Measurement of protein motion within a living cellular environment will enable dissection of key interactions among proteins, however, attempts to measure protein motion are typically limited by the low spatial and temporal resolution of existing experimental platforms. Here, we describe a high-throughput single-molecule imaging platform that measures protein motion in living cells. We demonstrate the application of this platform by studying the dynamics of steroid hormone receptors and explore the pharmacology of compounds that affect estrogen receptor (ER) activity. Using our high-throughput single-molecule tracking (htSMT) platform, we screened 5,067 bioactive molecules, identifying multiple proteins and signaling pathways which perturb ER dynamics. We further deployed htSMT to characterize the impact of known ER modulators on ER protein dynamics, uncovering a correlation between ER dynamics and the ability of ER antagonists to suppress cancer cell growth. SMT provides a novel platform capable of measuring real-time

target engagement within the living cellular environment. Our results support the view that this tool will prove uniquely valuable in measuring the dynamic interactions among proteins and will prove powerful for the identification of novel therapeutics.

Introduction

Both the activity and mobility of proteins within the crowded cellular environment are profoundly influenced by interactions with their surroundings[1–3]. Under these conditions, where diffusion is no longer well described by the Stokes radius of the protein monmer[4], changes in protein motion might be expected to correlate closely with changes in the activity of these proteins. The development of increasingly sophisticated live-cell microscopy techniques, including early ensemble methods like fluorescence recovery after photobleaching (FRAP) and fluctuation correlation spectroscopy (FCS), have informed our understanding of protein dynamics in cellular biology[5]. A myriad of technical improvements, such as enhanced labeling methods[6,7], better live-cell compatible fluorophores[8], new forms of light microscopy[9], dramatic increases in computational power[10], and the addition of machine learning approaches to data analysis[10,11] have together enabled a new era of imaging-based studies across biological contexts[3,5,12].

In single molecule tracking (SMT), a fluorescently labeled protein of interest is imaged at high spatiotemporal resolution to track its motion in a live cell[10]. The information embedded in these trajectories has been used to investigate diverse cellular phenomena including protein oligomerization state and function[13,14], inter-organelle communication[15], nuclear organization[16], and transcription regulation[17]. Of particular utility are “fast-SMT” approaches which use high frame rates and stroboscopic illumination to minimize motion-induced blurring, and hence can measure diffusive states over a large dynamic range[18,19]. Specifically, proteins that move rapidly

47 throughout the aqueous compartments of the cell are often missed in alternative tracking
48 approaches, biasing the resulting data. Furthermore, SMT in general, and fast-SMT in particular,
49 has not been adapted to a high-throughput setting that would enable the analysis of complex,
50 multi-component systems, or the identification of compounds that affect protein motion.

51 Steroid hormone receptors (SHRs) are a class of transcription factors that play crucial roles in
52 normal human development and in disease pathogenesis. SHRs like the estrogen receptor (genes
53 ESR1 and ESR2), androgen receptor (AR), and progesterone receptor (PR), as examples,
54 contribute decisively to the acquisition of secondary sex characteristics, while the glucocorticoid
55 receptor (GR) helps to orchestrate both metabolism and inflammation[20]. In their ligand-free state,
56 SHRs are kept sequestered in multiprotein complexes by the chaperone HSP90[21]. Canonically, in
57 the presence of hormone they dimerize and bind their cognate genomic response elements,
58 recruiting epigenetic modifiers and transcription machinery[21,22]. At the same time, steroid
59 hormone receptor-derived signals impose a large disease burden by promoting the growth of
60 breast cancers (ER)[23] or prostate cancers (AR)[20]; or by imposing immune and metabolic
61 dysfunction (GR)[20,24]. SHRs therefore provide an excellent proof-of-concept system to study the
62 relationship between protein dynamics and protein function due to the wealth of information and
63 reagents[23] already available for these systems as well as previous reports characterizing some
64 aspects of their cellular dynamics[17,25–28].

65 Here, we present the first industrial-scale, high-throughput, fast-SMT (htSMT) platform
66 capable of measuring protein motion in >1,000,000 cells per day. Using ER as a proof-of-
67 concept system, we demonstrate that high-throughput chemical screening using SMT is specific,
68 robust, and reproducible. htSMT can be used for classical drug discovery activities, including
69 compound library screening and the elucidation of structure-activity relationships (SAR).

70 Importantly, SMT can also be used to characterize both known and novel pathway contributions
71 to the ER protein interaction network.

72 **Results**

73 **Creation and validation of a high throughput SMT platform**

74 We developed a robotic system capable of handling reagents, collecting high-quality fast
75 SMT image series, processing time-ordered raw images to yield molecular trajectories, and
76 extracting features of biological interest within defined cellular compartments (Figure 1A). To
77 examine htSMT system performance across a broad spectrum of diffusion coefficients, we
78 generated three U2OS cell lines ectopically expressing HaloTag[6] fused proteins with well-
79 established behaviors in the cell. These HaloTag fusions allow the subsequent addition of bright
80 and photostable organic fluorophores like JF_{549}[8] which produce high signal spots to detect and
81 track. Histone H2B-Halo, which is predominantly incorporated into chromatin and therefore
82 effectively immobile over short timescales[19], was employed to estimate localization error. A
83 prenylation motif (Halo-CaaX) embedded in the plasma membrane exhibits moderate
84 diffusion[29]. Unfused HaloTag was chosen to represent the upper limit of cellular "free" diffusion.
85 Single-molecule trajectories measured in these cell lines yielded the expected diffusion
86 coefficients (Figure 1B). Using the immobile H2B-Halo trajectories, we found the localization
87 error of the htSMT system to be 39 nm (Extended data 1A), comparable to other benchmark
88 stroboscopic illumination datasets[19,30].

89 We then tested whether our htSMT platform can extract accurate molecular trajectories at
90 scale. We employed 384-well plates where free Halo, Halo-CaaX, and H2B-Halo cell lines were
91 mixed in equal proportions in each well. Imaging with a 94 µm by 94 µm field-of-view (FOV),
92 we achieved an average of 10 nuclei simultaneously (Figure 1C, Extended data 1B), enough that

93 most FOVs contained cells from each cell line. To limit ambiguity in cell assignment, we
94 considered only the trajectories that fell within nuclear-segmented regions. The probability
95 distribution of diffusion states cleanly distinguishes between the three cell types (Figure 1D).
96 More importantly, by looking at the single-cell state distribution profiles of 103,757 cells from
97 five separate 384-well plates, grouped by their distribution profile, we recovered highly
98 consistent estimates of protein dynamics at the single cell level (Figure 1E).

99 While single-cell measurements are powerful, the number of trajectories in one cell is
100 limited, and so estimates of diffusive states can be broad. Combining trajectories from multiple
101 cells, however, provides the expected distribution of diffusive states (Figure 1F). Moreover,
102 combining trajectories derived from many cells makes SpotOn[19] or State Array[30] analysis
103 possible, where as few as 10^3 trajectories permit satisfactory inference of the underlying
104 diffusion states. Only a few seconds of imaging per FOV yield enough trajectories (>10,000) to
105 accurately estimate protein dynamics, bringing the overall throughput of the platform to >90,000
106 FOVs per day, a rate of data acquisition that enables drug screening on a feasible timescale.

107 **Using htSMT to measure protein dynamics of SHRs**

108 Equipped with an htSMT system capable of measuring protein dynamics broadly, we sought
109 to understand how measuring protein motion can be used to characterize protein activity. SHRs
110 transition between inactive and active states via ligand binding (Figure 2A), and we hypothesized
111 that htSMT could capture these differences. We generated HaloTag fusion ER, AR, PR, and GR
112 cell lines in a U2OS cell background to minimize effects of comparing dynamics in different cell
113 types.

114 In the absence of hormone, all four proteins exhibit similar dynamic profiles: a small
115 immobile fraction and a large freely diffusing fraction with a 3.4 - 4.3 μm^2/sec average diffusion

116 coefficient (Figure 2B). No correlation between diffusion and monomeric protein size was
117 observed, highlighting the differences between cellular protein dynamics versus purified
118 systems. Upon addition of agonist, a dramatic increase in immobile trajectories is observed,
119 which we attribute to chromatin binding. We define the bound fraction (f_{bound}) for each SHR as
120 the fraction of trajectories diffusing less than 0.1 μm^2/sec (Figure 2B). Consistent with previous
121 findings, some SHRs had a higher proportion of bound molecules than others, both with and
122 without ligand[17]. The ligand-induced effect is most pronounced for ER, with 34% bound in basal
123 conditions and 87% bound after estradiol treatment (Figure 2B).

124 SHRs are highly selective for their cognate agonists in biochemical binding assays, which we
125 confirmed by measuring the dose-dependent change in dynamics as a function of agonist
126 concentration. The maximal increase in f_{bound} (Figure 2C) and decrease in free diffusion
127 coefficient (D_{free}; Figure 2D) differed between SHRs. The dose titration curves also showed
128 variable potencies (EC_{50}) for each SHR/hormone pair, with ER-estradiol being both the most
129 potent and most selective pair. Thus, SMT can precisely and accurately differentiate the
130 ligand/target specificity directly within the living cellular environment.

131 **Screening a diverse bioactive chemical set identifies known and novel modulators of ER**
132 **dynamics**

133 We next examined the specificity and sensitivity of our htSMT platform. We screened a
134 structurally diverse set of 5,067 molecules with heterogeneous biological activities against ER,
135 assessing change in f_{bound} at 1 μM compound versus DMSO (Figure 3). The screen was run twice
136 to assess reproducibility. Each compound measurement was averaged from SMT trajectories of
137 between 94 and 161 cells (25th to 75th percentiles; Extended Data 2A). This screen illustrates the
138 important advantages of our htSMT platform over more manual lower-throughput approaches.

139 From plate to plate, the assay window for the screen was robust[31] (Extended Data 2B ; average
140 Z'-factor = 0.79) and the measured potency of the control estradiol in each instance remained
141 within three-fold of the mean (Extended Data 2C and 2D) and the distribution of negative control
142 wells centered tightly on zero (Extended Data 2E). Of the 30 compounds we identified from the
143 bioactive set that we expected to modulate ER, either as agonists or antagonists[23,32], all
144 significantly increased f_{bound} measured by SMT, including notable examples such as 4-
145 hydroxytamoxifen, fulvestrant, and bazedoxifene (Figure 3).

146 **Cellular ER dynamics elucidate structure-activity relationships (SAR) of ER**
147 **modulators**

148 Our screen revealed that, surprisingly, all the known ER modulators—both agonists like
149 estradiol and potent antagonists like fulvestrant—caused an increase in f_{bound}. We therefore
150 characterized a subset of selective ER modulators (SERMs) and selective ER degraders (SERDs)
151 in more detail. These molecules all bind competitively to the ER ligand binding domain[23]. As in
152 the bioactive screen, both SERDs and SERMS increased f_{bound} (Figure 4A) and slightly decreased
153 measured D_{free} (Extended Data 3A), with potencies ranging from 9 pM for GDC-0927 to 4.8 nM
154 for GDC-0810 (Figure 4B). Despite different physical-chemical properties, all five increased
155 f_{bound} within minutes of compound addition (Figure 4C, Extended Data 3B), with no evidence of
156 transient diffusive states (Extended Data 3C). Presumably, ER dissociation from the chaperone
157 complex, dimerization, and chromatin binding occur on rapid and seemingly comparable
158 timescales. Since we cannot distinguish individual steps in these transitions, we consider the on-
159 rate of the entire process to have the effective rate constant k^*_{on}. Importantly, selective
160 antagonists of AR and GR did not induce significant modulation of ER dynamics, further

161 highlighting the utility of htSMT in characterizing the specificity of interactions between small
162 molecule modulators of protein function and their cognate targets (Extended data 3D).
163 Interestingly, SERMs 4-hydroxytamoxifen (4OHT) and GDC-0810 show lower maximal
164 increases in f_{bound} compared with the SERDs fulvestrant and GDC-0927 (Figure 4D). Similar
165 effects have been described previously using fluorescence recovery after photobleaching[27]
166 (FRAP), which we confirmed using our Halo-ER cell line (Figure 4E). The delay in ER signal
167 recovery after two minutes in FRAP was consistent with the changes in f_{bound} measured by SMT
168 (Figure 4F). Although FRAP was used to measure these f_{bound} differences, the technique suffers
169 from challenges in scalability and depends heavily on prior assumption of the underlying
170 dynamical model in the sample. Our instruments, however, permit detailed characterization of
171 the potency of 4OHT and GDC-0810 relative to other ER ligands in their ability to increase ER
172 chromatin binding.
173 Neither FRAP nor htSMT can discriminate between recovery driven by an increase in
174 residence time (decreasing k^*_{off}) or increasing the rate of chromatin binding (increasing k^*_{on}),
175 either of which would result in increasing f_{bound}. By changing SMT acquisition conditions to
176 reduce the illumination intensity and collect long frame exposures, only immobile proteins form
177 spots. Under these imaging conditions, the distribution of track lengths provides a measure of
178 relative residence times[17,33–35]. Both agonist and antagonist treatment led to longer binding times
179 compared to DMSO, suggesting that ligand binding decreases k^*_{off} (Figure 4G, Extended Data
180 3E). Consistent with FRAP, estradiol, GDC-0927, and fulvestrant show longer binding times
181 compared with other ER modulators. Using f_{bound} and k^*_{off} measurements, one can infer the k^*_{on}.
182 In all cases the changes in dissociation rate are not proportional to the increase in f_{bound}, and so
183 ligand-imposed increases in k^*_{on} likely contribute to the observed change in the chromatin-

184 associated ER fraction (Extended Data 3E). These data are consistent with a model wherein ER
185 rapidly binds to chromatin irrespective of which molecule occupies the ligand binding domain,
186 but some ligands induce a conformation that can be further stabilized on chromatin by cofactors.
187 Consequently, these data support the hypothesis that ER may engage chromatin in
188 mechanistically different ways[27]. An efficacious ER inhibitor may promote rapid and transient
189 chromatin binding that fails to effectively recruit necessary cofactors to drive transcription[25].

190 **htSMT can define relevant structure activity relationships for ER antagonists**

191 As the name implies, next-generation ER degraders like GDC-0927, AZD9833, and GDC-
192 9545 were optimized to enhance degradation of ER[27,36]. We indeed observed compound-induced
193 ER degradation via immunofluorescence, both in established breast cancer model lines and our
194 U2OS ectopic expression system (Figure 5A, Extended Data 4A). Structural analogs of GDC-
195 0927 have been reported and optimized for ER degradation, however the correlation between ER
196 degradation and cell proliferation is poor[23,37] (Figure 5B, Extended Data 4B-D). We
197 hypothesized that by measuring protein dynamics we might obtain more precise measurements
198 of inhibitory activity than can be achieved by assessing protein degradation. We therefore
199 determined the potency and maximal effect of structural analogues of GDC-0927 using htSMT.
200 Overall, these analogues exhibited a potency range of 15 pM to 12 nM and increased ER f_{bound} by
201 0.4 to 0.56 (Figure 5C). Small changes in the chemical structure produced measurable changes in
202 both compound potency and maximal efficacy as determined using SMT.

203 We compared the potencies of GDC-0927 and analogues determined either via ER
204 degradation or SMT, with the ability of each of these compounds to block estrogen-induced
205 breast cancer cell proliferation. Potency assessed by ER degradation was not a good predictor of
206 potency in the cell proliferation assay (Figure 5B). By contrast, SMT measurements of f_{bound}

207 strongly correlate with cell viability (Figure 5D; R^2 of 0.83 for T47d and 0.84 for MCF7).
208 Intriguingly, SMT EC_{50} values were on average 10-fold lower than those observed in the cell
209 growth assay, suggesting that SMT may be sensitive enough to permit the selection of chemical
210 series which would not show effects in at least some other cellular assays, enabling the
211 identification of starting points for medicinal chemistry that could not be obtained by other
212 methods. This correlation between effects on protein dynamics (f_{bound}) and protein function
213 (suppression of cell proliferation) coupled with the throughput of the SMT system make this an
214 attractive approach for the identification of protein modulators with novel properties.

215 **Individual pathway interactors show unique phenotypes related to their effects on ER**
216 **motility**

217 In addition to known ER active modulators, many other compounds in our bioactive library
218 provoked easily measurable changes in f_{bound}. To define a threshold for calling a molecule from
219 the screen "active", we selected 92 compounds with different magnitudes of change in f_{bound} to
220 retest in a dose titration (Extended Data 5A, B). We found that a 5% change in f_{bound} was
221 sufficient to reproducibly distinguish active compounds. Using this approach, we identified 239
222 compounds in the bioactive library that affected the ER mobility (Figure 3). Among these
223 compounds, the correlation between the two screen replicates was high ($R^2 = 0.92$) and the level
224 of activity was reproducible (the slope for active molecules was 0.94). Some active compounds
225 could be clustered based on scaffold homology, but most clusters consisted of one or only a few
226 members (Extended Data 5C, 5D). Structural clustering was employed to identify known ER
227 modulators where the vendor-provided annotation was poorly defined (Extended data 5C). Our
228 results demonstrate that htSMT is reproducible and robust when screening large collections of
229 molecules.

230 Most active molecules from the screen were not structurally related to steroids (Extended
231 Data 5C, D). On the other hand, many compounds could be grouped based on their reported
232 biological targets or pathways (Figure 6A, Extended Data 6A, B). For example, heat shock
233 protein (HSP) and proteasome inhibitors consistently increased f_{bound}, whereas cyclin dependent
234 kinase (CDK) and mTOR inhibitors decreased f_{bound}. Though many CDK inhibitors lack within-
235 family specificity[38] (Extended Data 6A, pan-CDK), we found that CDK9-specific inhibitors
236 more strongly affected ER dynamics than did CDK4/6-specific inhibitors. Furthermore, as with
237 selective AR and GR antagonists, inhibitors targeting ALK, BTK, and FLT3 kinases that have
238 not been shown to interact with ER have no impact on ER dynamics when assessed using SMT
239 (Figure 6A).
240 For the inhibitors of cellular pathways we identified, we used a dose titration to better
241 characterize the effect of each on ER dynamics. Potencies ranged from the sub-nanomolar to low
242 micromolar (Figure 6B), similar to the reported potencies of these compounds against their
243 cellular targets[39–50]. Additionally, we tested these molecules against AR (Extended Data 6C) and
244 PR (Extended Data 6D). Each SHR differed meaningfully from the others in terms of the
245 response to compounds identified through an ER-focused screening effort. Again, the magnitude
246 of ER SMT effect was largely consistent within a target class (Figure 6B, Extended Data 6A-D).
247 The finding that structurally distinct compounds exhibited similar effects based on their
248 biological targets favors the view that these biological targets must themselves interact with ER,
249 and that the compounds therefore affect ER dynamics indirectly. HSP90 is a chaperone for many
250 proteins, including SHRs. In the canonical model, hormone binding releases the SHR-HSP90
251 complex. Indeed, HSP90 inhibitors increased f_{bound} for ER, AR, and PR, consistent with the
252 hypothesis that one function of the chaperone may be to adjust the equilibrium of SHR binding

253 to chromatin (Extended data 6B-D). Proteasome inhibition also leads to ER immobilization on
254 chromatin[28], which aligns with the results that we obtained in our htSMT screen of bioactive
255 compounds. ER has been shown to be phosphorylated by CDK[51], Src[52], or GSK-3 through
256 MAPK and PI3K/AKT signaling pathways[53], and therefore inhibition of these pathways could
257 reasonably be expected to affect ER dynamics measured using SMT. While CDK inhibition led
258 to an increase in ER mobility, inhibition of PI3K, AKT, or other upstream kinases showed no
259 effect (Figure 6A).

260 Interestingly, SMT dynamics of an ER triple point mutant engineered to lack previously
261 defined phosphorylation sites important for transactivation[53] (S104A/S106A/S118A) were
262 affected by CDK and mTOR pathway inhibitors (Extended data 7), suggesting that additional
263 phosphorylation sites can mediate the effects of CDK9 and PI3K/AKT signaling, or that other
264 molecular targets of CDK and PI3K/AKT can act indirectly to alter the motion of ER. The
265 change in ER protein dynamics for characterized pathway inhibitors such as those targeting CDK
266 and mTOR is subtle but consistent across compounds, suggesting biological meaning in these
267 observations and highlight the need for accurate and precise SMT measurements. Hence htSMT
268 screening offers the promise of providing comprehensive pathway interaction information.

269 Since SMT can identify compounds that act either directly on a fluorescent target, or through
270 some intermediary process, we sought to distinguish between these alternative modes of action.
271 We hypothesized that by investigating the rate at which changes in protein motion emerge, SMT
272 could be used to distinguish direct versus indirect effects on ER activity. Given the live-cell
273 setting of SMT, we configured a data collection mode that allows for measurement of protein
274 dynamics in set intervals after compound addition (kinetic SMT or kSMT). Both ER agonists
275 and antagonists rapidly induce ER immobilization on chromatin when measured in kSMT ($t_{1/2}$ =

276 1.6 minutes for estradiol; Figure 4C). On the other hand, HSP90 inhibitors like ganetespib and
277 HSP990 exhibit a delay of 5 to 7 minutes before alterations in ER dynamics appear, after which
278 we observed an increase in f_{bound} with a $t_{1/2}$ of 19.3 and 17.5 minutes, respectively. The overall
279 effect of these compounds reached a plateau after an hour (Figure 6C). Proteasome inhibitors,
280 e.g. bortezomib and carfilzomib, acted even more slowly, with changes in ER dynamics
281 emerging only after 40 minutes, and slowly increasing over the four-hour measurement window
282 (Figure 6D). Hence this exploration of SMT kinetics represents an important tool that can
283 facilitate differentiation between on-target and on-pathway modulators. We believe that this
284 approach will permit, for example, rapid mechanistic characterization of active compounds in a
285 drug discovery setting.

286 To further differentiate the effect of pathway inhibitors on ER protein dynamics, we sought
287 to characterize relative ER residence times for each such molecule. Estradiol, SERMs, and
288 SERDs all increased residence times and thus likely also increased the rate of ER association
289 with chromatin (Figure 4, Extended Data 3E). By contrast, while HSP90 inhibition by HSP990
290 and ganetespib resulted in an increase in f_{bound}, we observed a decrease in the total number long
291 binding events by two- and four-fold, respectively, while the binding times were similar to that
292 observed with DMSO alone (Figure 6E). These results suggest HSP90 inhibition primarily
293 increases k^*_{on} while leaving k^*_{off} largely unaffected. On the other hand, inhibition of the
294 proteasome led to an increase in both the number and duration of long binding events. These
295 results demonstrate that ER-chromatin binding can be modulated by changing the rate of
296 association or disassociation, and that the inhibition of specific cellular partners can affect these
297 rates differentially. Taken together with the different kinetics for direct ER, HSP90, and

298 proteasome modulators, our data suggest that each class of molecule alters ER dynamics through
299 distinct mechanisms.

300 **Discussion**

301 Many, and perhaps most, pathways that regulate the fundamental biochemistry of cells
302 depend upon the interaction of protein sensors with protein effectors that engage transiently to
303 trigger a change in cell physiology. Although the fundamentals of this process have long been
304 appreciated, biochemical investigation of these protein interactions has typically required *in vitro*
305 reconstitution or has been interrogated through pull-down assays after cell permeabilization.
306 Here we report the application of super-resolution fluorescence microscopy as a means of
307 visualizing protein motion in large numbers of live cells, and under circumstances where the
308 effect of small molecule inhibitors can be assessed quantitatively.

309 Previously, the ability to evaluate protein motion has been limited to ensemble measurements
310 such as FRAP, or to SMT performed using custom microscope configurations capable of
311 analyzing small numbers of cells. To explore the broader utility of SMT for evaluating biological
312 processes in living cells, we developed a highly automated platform capable of examining more
313 than 1,000,000 cells per day in a robotic system that acquires high-quality imaging data and
314 performs automated analysis to extract critical parameters that describe protein dynamics. In the
315 present manuscript, we demonstrate the capabilities of the htSMT system by analyzing the
316 behavior of SHRs, a class of sensors that mediate hormone-induced modulation of gene
317 expression.

318 Our htSMT analysis documents the very rapid immobilization of SHRs on chromatin in
319 living cells exposed to steroid ligands. The technique has proved to be highly quantitative,
320 effectively evaluating ligands whose potency differ by more than four orders of magnitude, and

321 readily characterizing differences in both the sensitivity and the selectivity of the steroid receptor
322 family. These observations prompted us to explore htSMT as a tool for screening thousands of
323 bioactive compounds, yielding immediately important results. First, we showed that automated
324 screening of ER dynamics using htSMT permitted identification of all 30 steroid ligands from a
325 library of 5,067 bioactive compounds. Second, we showed that the potency of these steroid
326 ligands with respect to alterations in ER dynamics varied across a thousand-fold range. Among
327 those molecules known to behave as inhibitors, the change in ER dynamics correlated closely
328 with the ability of these compounds to block estrogen-induced proliferation of estrogen-
329 dependent breast cancer cells, demonstrating the ability of htSMT to document structure-activity
330 relationships in a chemical series. Since our analysis relies only on detection of changes in
331 protein dynamics, we believe that this approach will prove broadly useful in screening libraries
332 of compounds to identify starting points for the development of new therapeutics. Third, our
333 analysis identified 209 non-steroidal molecules that affect ER dynamics, almost certainly by
334 altering the behavior of other proteins that themselves interact with ER or the network of ER-
335 interacting proteins in living cells.

336 The observation that by screening large libraries of bioactive compounds htSMT can define
337 networks of biochemical signaling pathways deserves further explication. Protein dynamics in
338 the cell are not governed by singular interactions between any two proteins but by biochemical
339 networks within the cell that intersect with the protein under observation. Our work enables
340 construction of a hypothetical interaction network connecting nodes involving different proteins,
341 the identities of which were deduced based on the impact of known inhibitors on the dynamics of
342 steroid receptors (Figure 6F). More experiments are necessary to determine which connections
343 represent direct physical interactions and which occur through intermediaries. Of course, many

344 prior studies already support the identification of these protein nodes as part of a regulatory
345 network affecting the ER. However, few protein signaling systems have been elucidated in the
346 same detail as the SHRs. We believe that identifying cellular interaction networks through
347 htSMT will provide an important foundation for the broader understanding of biochemical
348 regulatory mechanisms. For example, CDK4/6 inhibitors are co-administered with SERDs and
349 SERMs to improve therapeutic outcomes[54,55]. CDK4/6 inhibition only minimally affects ER
350 dynamics in SMT (Figure 6A), supporting the view that the combination of CDK4/6 inhibition
351 with ER antagonists functions through a non-redundant ER-independent mechanism[56].
352 Most cell-based assays cannot easily be configured for kinetic analysis of treatment effects as
353 these typically involve fixed endpoint readouts. With such endpoint assays, biochemical
354 feedback and compensatory mechanisms often confound interpretation of the direct effect of a
355 change in treatment conditions. SMT, however, when implemented in a high-throughput system
356 that exhibits consistency over long time intervals, permits kinetic analysis of treatment effects on
357 protein dynamics with high reliability. Such kinetic analyses help to define pathway cascades; in
358 a first instance, they can be used to rapidly identify compounds that likely engage directly with a
359 therapeutic target.
360 Mechanistically, an increase in f_{bound} provoked by a change in cell conditions suggests that
361 molecular interactions with the protein being analyzed have been stabilized (that is, either made
362 more likely, or more durable), while a decrease in f_{bound} suggests precisely the opposite:
363 molecular interactions that have been made less robust. Interestingly, SERDs and SERMs, which
364 antagonize ER, cause an <u>increase</u> in nuclear bound fraction, likely via chromatin binding, in a
365 way that mimics what is seen with traditional ER agonists. Inhibition of HSP90 also produces a
366 marked increase in ER f_{bound}, though these binding events are more transient (Figure 6E).

367 Transcription factors are thought to find binding sites through free 3D diffusion, 1D sliding, and
368 transient, non-specific DNA binding[12,16,34,57]. ER antagonists may function by promoting ER
369 binding to non-specific decoy chromatin sites, thus reducing the amount of ER able to activate
370 transcription at ER-responsive genes[25,27]. Previous work has also shown that SERDs, and to a
371 lesser extent SERMs, induce an alternate conformation of ER, thereby inhibiting co-factor
372 recruitment[27]. If co-factors like CBP and p300 stabilize ER-chromatin binding, then efficacious
373 inhibitors might exhibit shorter binding times compared with agonist stimulation[27]. The SERMs
374 4OHT and GDC-0810 dramatically increase ER-chromatin binding frequency and only modestly
375 increase binding times; fulvestrant and GDC-0927 strongly increase both ER-chromatin binding
376 frequency and residence time. Further work is required to dissect the relationships that associate
377 ER dynamics with either agonism or antagonism.

378 Lastly, we note that fast-SMT, as implemented here, permits the rapid and sensitive
379 assessment of relationships between the structures of chemical inhibitors and their effects on a
380 fundamental property of protein regulatory elements, their dynamics in living cells. In our hands,
381 these measurements proved far more reliable in predicting the ability of an ER antagonist to
382 block cell proliferation than an ER degradation assay and did so at far lower compound
383 concentrations. Thus, SMT can identify promising compounds the activity of which might not
384 otherwise be measurable, provide insight into their mechanism(s) of action, and deliver results
385 within hours rather than days. While ER is a transcription factor, we suggest that the same
386 principles apply broadly to regulatory mechanisms and a collection of protein targets with
387 diverse function. In this context, we conclude that fast-SMT, conducted under circumstances
388 where tens of thousands of individual proteins in hundreds of cells can be rapidly interrogated,
389 will prove broadly applicable to the elucidation of biological mechanisms.

390 **Author Contributions**

391 D. A., H. P. B., D. T. M., & Y. T. conceived the research project; D. A., H. P. B., X. D., E. G.,
392 A. He., J. H., H. L., D. T. M., S. E. P., R. T., & Y. T. contributed to study design; H. C., K. F., E.
393 G., H. L., D. T. M., S. E. P., A. S., & R. T. performed experiments; H. C., E. G., H. L., D. T. M.,
394 A. S., & R. T. generated reagents; L. A., D. A., A. Ha, A. He., H. L., D. T. M., & R. T. analyzed
395 data; S. A., R. B., M. B., R. G., A. Ha, A. He, S. L. J., R. K., A. K., J. L., & L. M. designed and
396 wrote software; R. B., X. D., R. K., K. L., B. M., & D. T. M. designed and built hardware; D. A.,
397 H. P. B., R. B., J. H., A. K ., & R. K. supervised the work; L. A., D. A., A. He., H. L., D. T. M.,
398 S. E. P., & R. T. wrote the original draft; L. A., D. A., H. P. B, R. B., X. D., A. He., J. H., H. L.,
399 D. T. M., R. T., & Y. T. reviewed and revised of the original draft

400 **Acknowledgements**

401 The authors extend their deepest gratitude to all the employees and consultants of Eikon, past
402 and present, especially Caitlyn Bonilla, Tiffany Cheng, Michael Hirte, David Hoffman, Fedor
403 Ilkov, Yan Li, Edith Martinez-Soto, Eugene Masterov, Mai Nguyen, and Gregory Snyder. Their
404 tireless work enabled the experiments described here. We thank Roger Perlmutter, Yan Li,
405 Robert Tjian for helpful discussions and critical feedback on the direction of our investigation
406 and on the resulting manuscript. Eikon Therapeutics provided all funding.

407 **Declaration of interests**

408 The authors are employees and/or shareholders of Eikon Therapeutics.

409 **Figure captions**

410 **Main Figures**

411 **Figure 1.** Establishing a high throughput single molecule tracking platform

412 a) Schematic of the htSMT workflow.

413 b) Diffusion state probability distributions from three cell lines expressing Histone H2B-
414 Halo, Halo-CaaX, or Halo alone. Shaded bins represent the diffusive states characteristic
415 of each cell line.

416 c) Example field of view. Mixed H2B-Halo, Halo-CaaX and free Halo cell line single
417 molecule images (top) and reference Hoechst image (bottom). Insets show zoom-ins to
418 individual cells and to sequential frames of individual molecules. Image intensities are
419 equivalently scaled across panels.

420 d) Single-cell diffusive states extracted from (c), colored based on similarity to the H2B-,
421 CaaX-, or free-Halo dynamics reported in (b).

422 e) Heatmap representation of 103757 cell nuclei measured from a mixture of Halo-H2B,
423 Halo-CaaX, or Free Halo mixed within each well over 1540 unique wells in five 384-well
424 plates. Each horizontal line represents a nucleus. Cells were clustered using k-means
425 clustering and labels assigned based on the diffusive profiles determined in (b).

426 f) Ensemble state array of all trajectories recovered from a mixture of Halo-H2B, Halo-
427 CaaX, free Halo cells.

428 **Figure 2.** Comparison of dynamics in a panel of steroid hormone receptors

429 a) Cartoon illustration of SHR function. Under basal conditions, SHRs are sequestered in
430 complex with HSP90 and other cofactors. Upon ligand binding, the receptor dissociates
431 from the inactive complex, dimerizes, and binds to DNA.

432 b) Distribution of diffusive states for Halo-AR, Halo-ER, Halo-GR, and Halo-PR in U2OS
433 cells before and after stimulation with an activating ligand. The area in the shaded region
434 is f_{bound}. Shaded error bands represent S.D.

435 c) Selectivity of individual SHRs to their cognate ligand compared with other steroids, as
436 determined by f_{bound}. Error bars represent SEM.
437 d) Selectivity of individual SHRs to their cognate ligand compared with other steroids, as
438 determined by D_{free}. Error bars represent SEM.
439 **Figure 3.** Screen of bioactive compounds against ER shows reproducibility and robustness. The
440 repeatability of screening results was assessed over two biological replicates. The plot
441 shows the change in f_{bound} for ER from 5067 compounds. Compounds in magenta were
442 identified as active if their magnitude of change in f_{bound} when averaged across both
443 replicates was greater than ±0.05. Of the expected 30 positive control compounds, 26
444 significantly increased f_{bound} in both replicates (gray outline). Three compounds increased
445 f_{bound} but were only present in one replicate after filtering. Exemplified positive controls
446 including the agonist estradiol (1) and the antagonists fulvestrant (5), 4-OHT (6) and
447 bazedoxifene (7) are exemplified. A linear regression was fit to the magenta compounds
448 to determine slope and correlation.
449 **Figure 4.** Selective ER modulators and degraders induce DNA binding measurable through
450 htSMT
451 a) Diffusion state probability distribution for ER treated with 100 nM of exemplified
452 SERMs and SERDs. Shaded regions represent the S.D.
453 b) Change in f_{bound} as a function of a 12-pt dose titration of fulvestrant (5), 4-OHT (6),
454 GDC-0810 (8), AZD9496 (9), or GDC-0927 (10) with fitted curve. Compounds colored
455 as in (a). Error bars represent the SEM of three replicates.

456 c) Change in f_{bound} as a function of time after agonist or antagonist addition, fitted with a
457 single exponential. Compounds colored as in (a). Estradiol (1, green) and DMSO added
458 for comparison. Error bars represent SEM.
459 d) Maximum effect of SERMs and SERDs on f_{bound}. Each box represents quartiles while
460 whiskers denote the 5-95th percentiles of single well measurements, measured over a
461 minimum of four days with at least 8 wells per compound per day.
462 e) Fluorescence Recovery After Photobleaching of ER-Halo cells, treated either with
463 DMSO alone or with 100 nM SERM/D. Curves are the mean ± SEM for 18-24 cells,
464 colored as in (a). Error bands represent SEM.
465 f) Quantification of FRAP recovery curves to measure recovery 2 minutes after
466 photobleaching. Whiskers denote the 5-95th percentiles of single cell measurements.
467 g) Track length survival curve of ER-Halo cells treated either with DMSO alone or with
468 SERM/D. Track survival is plotted as the 1-CDF of the track length distribution; faster
469 decay means shorter binding times. *Inset* Quantification of the curves in (g), each point
470 representing the fraction of trajectories greater than 10 seconds for a single biological
471 replicate consisting of 3-10 wells per condition. Dashed line represents the median
472 fraction of trajectories lasting longer than 10 sec for Histone H2B-Halo, which represents
473 the upper limit of measurement sensitivity.
474 **Figure 5.** htSMT can be used to determine chemical structure-activity relationships
475 a) Example of GDC-0927 induced degradation of ER in different cell lines measured by
476 immunofluorescence against ER. Cells were exposed to compound for 24 hours prior to
477 fixation. Image pixel intensities are equivalently scaled.

478 b) Correlation of potency measured by ER degradation and cell proliferation in MCF7 cells
479 (black) and T47d cells (magenta) for compounds in the GDC-0927 structural series.
480 c) Change in f_{bound} across a 12-pt dose titration of compounds 11 through 16, colored by
481 structure. Points are the mean ± SEM across three biological replicates.
482 d) Correlation of potency measured by change in f_{bound} and cell proliferation in MCF7 cells
483 (black) and T47d cells (magenta) for compounds in the GDC-0927 structural series.
484 **Figure 6.** Bioactive molecules targeting pathways associated with ER affect its dynamics
485 a) Bioactive screen results with select inhibitors grouped and uniquely colored by pathway.
486 b) Change in f_{bound} across a 12-pt dose titration of three representative compounds targeting
487 each of HSP90, mTOR, CDK9 and the proteasome. Individual molecules are denoted by
488 specific shapes. Error bars represent SEM.
489 c) Change in f_{bound} as a function of time after compound addition. Estradiol treatment
490 (black) is compared to ganetespib (blue circles) and HSP990 (blue squares). Points are
491 bins of 4 minutes. Error bars represent SEM.
492 d) Change in f_{bound} as a function of time after compound addition. Estradiol treatment
493 (black) is compared to HSP90 inhibitors ganetespib (blue circles) and HSP990 (blue
494 squares); proteasome inhibitors bortezomib (red circles) and carfilzomib (red squares).
495 Points are bins of 7.5 minutes of htSMT data, marking the mean ± SEM. The shaded
496 region denotes the window of time used during htSMT screening.
497 e) Track length survival curve of ER-Halo cells treated either with DMSO alone, with
498 estradiol stimulation, or with 100 nM HSP90 or proteasome inhibition. Track survival is
499 plotted as the 1-CDF of the track length distribution; faster decay means shorter binding
500 times. *Inset* Quantification of the number of trajectories greater than length 2 as a

function of treatment condition. All conditions were normalized to the median number of trajectories in DMSO.

f) Diagram summarizing pathway interactions based on htSMT results for ER, AR, and PR.

Extended Data

Extended data figure 1. Characterization of htSMT system performance.

a) Distribution of localization error measured across multiple independent wells using Histone H2B-Halo cells. Median localization error of 39 nm.

b) Number of measurable nuclei in a 94 by 94 µm FOV. Each box plot is the distribution over wells in one 384-well plate.

Extended data figure 2. Screen of bioactive molecules produces robust data with good assay performance.

a) Boxplot showing the number of cell nuclei measured for each compound tested. Whiskers are the 1st and 99th percentiles.

b) Z'-factor analysis for the bioactive screen. Each point represents the Z'-factor of a single 384-well plate, measuring the difference between DMSO and 25 nM estradiol treatment. Plates with very low Z'-factors were removed from further analysis.

c) Dose titration of estradiol for each plate in the bioactive molecules screen fit with a logistic regression to determine potency.

d) EC_{50} values extracted from each curve fit in (c). Shaded region is a three-fold range in potency.

e) Distribution of change in f_{bound} for control DMSO wells.

523 **Extended data figure 3.** SERMs and SERDs decrease free diffusion and increase f_{bound} rapidly
524 after addition.

525 a) Normalized occupation of diffusive states (diffusion coefficient 0.2 – 100 μm^2/sec) for
526 100 nM SERD or SERM-treated samples compared with DMSO. Histograms are
527 normalized to integrate to 1. Shaded regions represent bin-wise standard deviations.
528 Curves are the average of 3-4 biological replicates, with 8 well replicates per condition.
529 b) Results from a single-exponential association fit to the data in Figure 4C.
530 c) Change in diffusive state distribution as a function of time after compound addition for
531 estadiol and fulvestrant. Each curve represents the mean of three biological replicates.
532 Shaded regions are the bin-wise standard deviation.
533 d) Change in f_{bound} of selective AR or GR antagonists from the bioactive screening set.
534 e) Table of results of the slow decay rate constant (k_{slow}) from SMT curve fits. Fits were
535 performed on the aggregate of three biological replicates. Taken together with the f_{bound}
536 determined in 4D, an upper limit of the inferred k_{on} can be calculated from the equaltion
537 assuming all bound molecules will have $k^*_{off} = k_{slow}$. Cells marked with an asterisk are
538 ones in which k_{slow} could not reliably be distinguished from photobleaching.

539 **Extended data figure 4.** GDC-0927 structural variants characterized by ER degradation or cell
540 proliferation assays.

541 a) Western blot of the ER-expressing breast cancer cell lines MCF7 and T47d compared to
542 ER expression in ER-null lines SK-BR-3 or U2OS. Samples were treated with fulvestrant
543 for 24 hours prior to lysis. Fulvestrant treatment leads to the degradation of ER, even
544 when fused to HaloTag.

545 b) Example compound dose titrations showing change in mean nuclear intensity as a
546 function of compound concentration.
547 c) Example of GDC-0927 effect on MCF7 breast cancer cell proliferation, compared with
548 Staurosporine as a positive control.
549 d) Example compound dose titrations measuring cell proliferation, normalized to DMSO-
550 treated cells, of cells treated with analogs of GDC-0927.
551 **Extended data figure 5.** Deeper investigation of bioactive screening data identifies cutoff for
552 active molecules.
553 a) Examples of compound effects on ER f_{bound} from a dose titration experiment. 92
554 compounds from the primary screen are ranked based on the magnitude of their effect.
555 Compounds colored in black repeatably showed dose-dependent changes; magenta
556 compounds were inactive in a dose titration.
557 b) Example dose titration of compounds of increasing overall change in ER f_{bound}.
558 c) Two replicates of the bioactive screen as in Figure 3. Active compounds are colored
559 based on structural scaffold.
560 d) A quantification of the number of compounds associated with any given cluster.
561 Singletons (cluster 21) represent the majority of active compounds
562 **Extended data figure 6.** Some pathway inhibitors modulating ER dynamics are specific to ER.
563 a) Change in f_{bound} of ER following treatment with inhibitors of HSP90, the proteasome,
564 mTOR, and CDK from the initial bioactive screen. CDK inhibitors were further stratified
565 into CDK4/6 inhibitors, CDK9 inhibitors, or inhibitors without strong selectivity for a
566 particular family (pan-CDK). Line represents the median for each target.

567 b) Change in f_{bound} of ER for 97 bioactive molecules, colored by their pathway annotation.
568 Compounds are plotted in their rank order based on their effect in ER. Error bars are the
569 SEM of three biological replicates.
570 c) Change in f_{bound} of AR for the same molecules from (b). Compounds are plotted in their
571 rank order based on their effect in ER. Error bars are the SEM of three biological
572 replicates.
573 d) Change in f_{bound} of PR for the same molecules from (b). Compounds are plotted in their
574 rank order based on their effect in ER. Error bars are the SEM of three biological
575 replicates.
576 **Extended data figure 7.** Dose titration plots of ER(S104A/S106A/S118A) with mTOR and
577 CDK9 compounds. Each point represents the mean and SEM of three biological replicates.

578 **Methods**

579 **Cell Lines**

580 U2OS (ATCC Cat. No. HTB-96), MCF7 (ATCC Cat. No. HTB-22), T47d (ATCC Cat. No.
581 HTB-133) and SK-BR-3 (ATCC Cat. No. HTB-30) were grown in DMEM (Cat. No. 1056601,
582 Gibco DMEM, high glucose, GlutaMAX Supplement, Thermofisher) supplemented with 10%
583 Fetal Bovine Serum (Cat. No. 16000044, Thermofisher) and 1% pen-strep (Cat. No 15140122,
584 Thermo Fisher) and maintained in a humidified 37 °C incubator at 5% CO_2 and subcultivated
585 approximately every two to three days.

586 **HaloTag-expressing cell lines**

587 For ER, AR, and PR-HaloTag fusions, mammalian expression vectors containing the fusion
588 gene under the control of a weak L30 promoter and containing a Neomycin resistance marker
589 were transfected into U2OS cells at 70% confluence using FuGENE 6 (Cat. No. E2691,

590 Promega). Transfected cells were selected with G418 (Cat. No. 10131027, Thermo Fisher) at
591 500 μg/mL, then clonally isolated. Clones expressing the desired fusion gene were determined
592 first by staining with 100 nM JF_{549}-HTL (Cat. No. GA1110, Promega) and 50 nM Hoechst
593 33342 and identifying clones with the expected distribution of JF_{549} signal. Between three and
594 six clones were subsequently tested using SMT conditions for response to a control compound,
595 and the most homogenous clones were subsequently expanded for further testing. Unless
596 otherwise specified, all experiments are with a single, clonally isolated cell line. Because U2OS
597 cells express GR endogenously, HaloTag was inserted right before the stop codon of endogenous
598 NR3C1 via homology-directed repair using CRISPR/Cas9. The HaloTag knock-in was validated
599 by imaging using HTL-JF_{646} staining and through DNA sequencing[58].

600 **Western Blot**

601 Cells were grown in the same conditions as described previously. $1.5x10^6$ cells were seeded
602 per well in a 6-well plate in DMEM overnight, followed by compound treatment (DMSO or
603 100nM fulvestrant) the following day for 24 hours. Cells are lysed in 200 μL 1X Cell Lysis
604 Buffer (catalogue number 9803, Cell Signaling). Protein lysate concentration is then determined
605 using BCA protein assay kit (Catalog number 23225, Pierce™ BCA Protein Assay Kit)
606 following manufacturer instructions. Capillary Western Immunoassay were performed using Jess
607 Protein Simple following manufacturer's instruction (protein simple, USA). Levels of αER
608 (1:100, RM-9101) were normalized to loading control β-tubulin (1:100, NC0244815 LI-COR
609 92642213, Thermo Fisher). The peaks were analyzed with the Compass software (Protein
610 Simple, USA).

611 **RNA-seq**

612 Cells were seeded into 12-well tissue-culture treated plates at densities of 250,000 cells
613 (U2OS-WT), 200,000 cells (U2OS-ER), or 300,000 cells (MCF7, SK-BR-3, T47d) per well. 24
614 hours later, cells were treated with estradiol at a final concentration of 25nM for the indicated
615 time-points (0 minutes, 10 minutes, 60 minutes, or 3 hours). To process cells for total RNA, cells
616 were washed twice with ice-cold PBS, lysed with 350uL Buffer RLT (Qiagen 79216), scraped
617 off the plate (Fisher 08100241), frozen on dry ice and stored at –20 degrees C. Cell lysates were
618 then thawed, homogenized using QIAshredder columns (Qiagen 79656), and processed through
619 the Qiagen RNeasy Micro kit (Qiagen 74004) using the standard protocol and including the
620 optional on-column DNase digestion step (Qiagen 79254). All samples had a RIN score of 10 by
621 TapeStation (Agilent 5067-5576). RNA sequencing libraries were prepared from total RNA by
622 Novogene (CA). In brief, mRNA was purified from total RNA using poly-T oligo-attached
623 magnetic beads and fragmented. First-strand synthesis was performed using random hexamer
624 primers, second-strand synthesis was performed using dTTP, and libraries were prepared after
625 end repair, A-tailing, adapter ligation, amplification, and purification. Libraries were sequenced
626 on an Illumina NovaSeq with paired 150 cycle reads. For data analysis, paired-end reads were
627 aligned to the hg38 reference genome using Hisat2 v2.0.5, featureCounts v1.5.0-p3 was used to
628 count the number of reads mapped to each gene, and differential expression analysis was
629 performed using DESeq2 (1.20.0).

630 **Single Molecule Tracking Sample preparation**

631 Cells were seed on tissue culture treated 384-well glass-bottom plates at 6000 cells per well.
632 Seeded cells were then incubated at 37 °C and 5% CO_2 to allow adhesion overnight. For all SMT
633 experiments, cells were incubated with 5-100 pM of JF_{549}-HTL (Cat. No. GA1110, Promega)

634 and 50 nM Hoechst 33342 for an hour in complete medium. Cells were then washed three times
635 in DPBS and twice in imaging media, which is fluoroBrite DMEM media (Cat. No. A1896701,
636 Thermo Fisher) supplemented with GlutaMAX (Cat. No. 35050079, Thermo Fisher) and the
637 same serum and antibiotics as growth media. Where appropriate, compounds were serially
638 diluted in an Echo Qualified 384-Well Low Dead Volume Source Microplate (0018544,
639 Beckman Coulter) to generate dose-titration source material. Compounds were administered at a
640 final 1:1000 dilution in cell culture medium. Each dose of a compound has at least 2 replicates
641 per plate and 3 plate replicates, 20 DMSO control wells and 2 no dye control wells were
642 randomized across each plate. Unless otherwise specified, compounds were allowed to incubate
643 for an hour at 37 °C prior to image acquisition.

644 **Image Acquisition**

645 Unless otherwise stated, all image acquisition using SMT was performed on a custom-built
646 HILO microscope based on a Nikon Ti2, motorized stage, stage top environmental chamber
647 (OKO labs), quad-band filter cube (Chroma), custom laser launch with 405 nm, and 561 nm
648 wavelengths, delivering >10 mW and >150 mW of power to the back focal plane of the
649 objective, respectively. Fluorescence emission was passed through a high-speed filter wheel
650 (Finger Lakes Instruments) and collected with a backlit CMOS camera (Prime 95b, Teledyne).
651 Images were acquired with a 60X 1.27 NA water immersion objective (Nikon). Environmental
652 chamber was set to 37° Celsius, 95% humidity, and 5% CO_2. For each field of view, 200 SMT
653 frames were collected at a frame rate of 100 Hz, with a 2 msec stroboscopic laser pulse. 10
654 frames of the Hoechst channel were collected at the same frame rate for downstream registration
655 of trajectories to nuclei.

656 **Image Analysis**

657 Image acquisition produced one JF_{549} movie and one Hoechst per field of view. The JF_{549}
658 movie was used to track the motion of individual JF_{549} molecules, while the Hoechst movie was
659 used for nuclear segmentation. Tracking was accomplished in three sequential steps – detection,
660 subpixel localization, and linking – using a combination of existing methods. Briefly, spots were
661 detected using a generalized log likelihood ratio detector[59]. After detection, the estimated
662 position of each emitter was refined to subpixel resolution using Levenberg-Marquardt fitting[60–
663 62] with an integrated 2D Gaussian spot model[63] starting from an initial guess afforded by the
664 radial symmetry method[64]. Detected spots were linked into trajectories using a custom
665 modification of a hill-climbing algorithm[10,65]. The same detection, subpixel localization, and
666 linking settings were used for all movies used in this manuscript.

667 For nuclear segmentation, all frames of the Hoechst movie were averaged to generate a mean
668 projection. This mean projection was then segmented with a neural network trained on human-
669 labeled nuclei [66]. Each spot was assigned to at most one nucleus using its subpixel coordinates.

670 To recover dynamical information from trajectories, we used state arrays[30], a Bayesian
671 inference approach, with the "RBME" likelihood function and a grid of 100 diffusion
672 coefficients from 0.01 to 100.0 $\mu m^2 s^{-1}$ and 31 localization error magnitudes from 0.02 to 0.08
673 μm. After inference, localization error was marginalized out to yield a one-dimensional
674 distribution over the diffusion coefficient for each field of view. For single-cell analysis, we
675 performed SMT and nuclear segmentation on a mixture of U2OS cells bearing H2B-HaloTag,
676 HaloTag-CaaX, or free HaloTag. We then evaluated the marginal likelihood of each of a set of
677 100 diffusion coefficients on the set of trajectories within each segmented nucleus[30]. These
678 marginal likelihood functions were clustered with k-means (3 clusters), and the marginal

679 likelihood functions for each cell were ordered by their cluster index to produce the heat map. To
680 estimate the fraction bound (f_{bound}), we integrated the state array posterior distribution below 0.1
681 $\mu m^2 s^{-1}$. To estimate the free diffusion coefficient (D_{free}), we computed the mean of the posterior
682 distribution above 0.1 $\mu m^2 s^{-1}$.

683 **Data analysis**

684 Tracking results from the automated processing pipeline were analyzed using KNIME or
685 Spotfire (TIBCO). Individual f_{bound} or D_{free} measurements were associated with experimental
686 metadata and aggregated by condition. Change in f_{bound} was calculated as the difference between
687 the f_{bound} of each well and the median f_{bound} of DMSO in the same plate. Wells that had no cells in
688 the field of view or in which the field of view was out of focus were omitted from further
689 analysis. Compounds were assessed for assay interference using the median fluorescence
690 intensity of the tracking channel and omitted if it was more than 3 standard deviations higher
691 than the median intensity of the DMSO wells. Similarly, plates where the active and negative
692 controls could not be clearly resolved or where the significantly deviated from the performance
693 of the rest of the screen were removed from further analysis. Finally, compound with a variance
694 more than three standard deviations higher than the average compound variance (41 compounds;
695 0.08%) were removed from downstream analysis. Z'-factor between the active controls on a
696 plate and DMSO was calculated as previously described[31]. EC_{50} values were calculated in Prism
697 (GraphPad) by first log-transforming the molecule concentrations and then fitting to a four-
698 parameter logistic curve.

699 **Clustering active molecules**

700 Chemical structure-based clustering was performed on molecules identified as active (239 in
701 total). Molecular frameworks were computed as described by Murcko et al and as implemented

702 in Pipeline Pilot[67]. Molecular frameworks were clustered using functional class fingerprints
703 (FCFP_4) with a similarity threshold cut-off of 0.3 Tanimoto distance. A total of 21 clusters
704 were obtained with singletons being the major class (124 molecules). The next largest group was
705 the flavone class represented by 27 members, followed by a couple of diverse classes within the
706 steroidal class with 14 and 20 members respectively. The other category is the stilbene class with
707 7 members representing tamoxifen as one of the members. The remaining actives (47 molecules)
708 were grouped into one 3-membered cluster and all the others with 2 members per cluster.

709 **Kinetic Experiments**

710 Cells were seeded into a 384-well plate the day before, dyed, and washed as described above.
711 1 well with 25 FOVs per well were taken as a baseline reading. Then, while imaging, compound
712 was manually added to each well to a final concentration of 100 nM. Data was then collected for
713 20 wells. A pause was included between each FOV such that the entire imaging regime covers
714 the assay window. Change in f_{bound} was determined per-well relative to t=0.

715 For assays extending to 4 hours, the plate was imaged twice with 8 FOVs per well with
716 different FOV locations per readthrough to prevent photobleaching from impacting data. All data
717 presented represents was performed in three different biological replicates.

718 **Residence Time Imaging**

719 Sample preparation and execution of residence time imaging experiments were conducted in
720 a similar manner to the single molecule tracking assay described above with a few exceptions.
721 Samples were dyed with 1 – 10 pM JF_{549} (Promega) and 50 nM Hoechst 33342 for an hour. 400
722 frames per field of view were collected with a camera integration time was set to 250 msec, and
723 laser sources reduced to 5 mW at the objective. During image acquisition, lasers were on

724 continuously. Compound incubation ranged from 1 to 4 hours. At least 8 well replicates were
725 collected per condition.

726 **Residence Time analysis**

727 Image processing, including spot detection, localization, and track reconnection were
728 performed using the same methods described above. Because residence time imaging selectively
729 tracks slow-diffusing molecules, individual localizations were limited to a 300 nm maximum
730 displacement for individual jump reconnections. Sets of trajectories for each field of view were
731 binned into 1-CDF distributions as previously described[34] and fit to a two exponent decay model
732 $CDF(t) = A(Fe^{-k_{fast}t} + (1-F)e^{-k_{slow}t})$.

733 **Fluorescence Recovery After Photobleaching**

734 Images were acquired on a custom-built HiLo microscope as described above with a Spectra
735 Light Engine RS-232. Stimulation was directed using a miniscanner coupled with a Coherent
736 OBIS 561nm 100 mW laser. All imaging was performed using a 60X 1.27 NA water immersion
737 objective (Nikon). All experiments were performed at 37° Celsius. For FRAP experiments, Cells
738 were seeded into a 384-well plate the day before, labeled with 50 nM HTL-JF_{549}, and washed as
739 described above. Compound was added to 100 nM final an hour before imaging. Then, a pre-
740 bleach image was acquired by averaging 10 consecutive images. Then 8-10 regions were
741 bleached (2 background, 6-8 cells) and 2 regions in cells were unbleached. Regions that were
742 bleached were bleached at 10% power without scanning. For the next 30 seconds, an image was
743 acquired every 200 ms, then every 1 second for 2 minutes. The background-subtracted average
744 intensity was measured in the region of interest over time and normalized to the average of the
745 fluorescence in the baseline images, then normalized to the unbleached regions to account for

746 readout-induced photobleaching of fluorophores. Data from 18-24 cells were pooled per
747 experiment for 3 biological experiments.

748 **Immunofluorescence**

749 Cells were grown in conditions as described previously. Cells were seeded in glass bottom
750 384-well plates coated with 0.05mg/ml PDL (Cat. No. A3890401, Thermofisher) at 6000 cells
751 per well for Halo- ER U2OS cells and 8000 for MCF7 and T47d cells. Cells were grown
752 overnight followed by compound treatment on the second day for 24 hours at 37 °C and 5%
753 CO_2. Compounds were serially diluted in an Echo® Qualified 384-Well Low Dead Volume
754 Source Microplate (0018544, Beckman Coulter) to generate a 21-point dose response at 1:3
755 dilution starting from a concentration of 10mM. Compounds were administered at a final 1:1000
756 dilution in cell culture medium. An 8 to 12-point dose response was selected based on the
757 potency of each compound. Each concentration was replicated at least once per plate and has at
758 least 2 plate replicates. Cells were fixed by addition of paraformaldehyde (Cat. No. 15710-S;
759 Electron Microscopy Sciences), with a final concentration of 4% for 20 minutes. Cells were then
760 permeabilized using blocking buffer containing 1% bovine serum albumin and 0.3% Triton-
761 X100 in 1x PBS for an hour at room temperature. Immunofluorescent staining of ER was carried
762 out using αER antibody (1:500, RM-9101) diluted in the same blocking buffer for 1 hour at room
763 temperature. Extensive washing with PBS was performed prior to secondary antibody staining.
764 Secondary antibody staining was carried out using Alexa fluor 488 conjugate anti-rabbit IgG
765 (1:1000, Cat. No. A32731, thermos Fisher) for an hour. Nuclear staining was carried out using
766 Hoechst 33342 solution at 1mg/ml. Imaging of immunofluorescence was done using the
767 ImageXpress Micro (Molecular Devices) at 10x magnification and 4 field-of-view per well.

768 Fluorescence intensity within the nucleus were quantified using CellProfiler[68]. All analysis and
769 curve fitting were carried out using Prism with DMSO as a baseline.

770 **Cell proliferation**

771 Cells were grown and seeded in conditions as described above. Cells were seeded in 384-
772 well plates (Cat. No. 353963, Corning) at 1000 cells per well for Halo-ER U2OS, 1200 cells for
773 SK-BR-3 and 1800 cells for MCF7 and T47d. Cells were grown overnight, then treated with
774 compounds the following day. Compound concentration and administration are the same as
775 described previously for the immunofluorescence assay. Plates are scanned in the IncuCyte live-
776 cell analysis system (Sartorius) at 24-hour intervals for a total of 5 days using phase contrast.
777 Cell proliferation quantification was carried out by the built-in analysis function using whole
778 well confluency mask. All analysis and curve fitting were carried out using Prism with DMSO as
779 a baseline.

780 **References**

781

782 (1) Heo; Sugita; Feig. Protein Assembly and Crowding Simulations. *Curr Opin Struct Biol*
783 **2022**, *73*. https://doi.org/10.1016/j.sbi.2022.102340.
784 (2) Guin, D.; Gruebele, M. Weak Chemical Interactions That Drive Protein Evolution:
785 Crowding, Sticking, and Quinary Structure in Folding and Function. *Chem Rev* **2019**, *119*
786 (18), 10691–10717. https://doi.org/10.1021/acs.chemrev.8b00753.
787 (3) Shen, H.; Tauzin, L. J.; Baiyasi, R.; Wang, W.; Moringo, N.; Shuang, B.; Landes, C. F.
788 Single Particle Tracking: From Theory to Biophysical Applications. *Chem Rev* **2017**, *117*
789 (11), 7331–7376. https://doi.org/10.1021/acs.chemrev.6b00815.
790 (4) Skóra, T.; Vaghefikia, F.; Fitter, J.; Kondrat, S. Macromolecular Crowding: How Shape
791 and Interactions Affect Diffusion. *J Phys Chem B* **2020**, *124* (35), 7537–7543.
792 https://doi.org/10.1021/acs.jpcb.0c04846.
793 (5) Liu; Lavis; Betzig. Imaging Live-Cell Dynamics and Structure at the Single-Molecule
794 Level. *Mol Cell* **2015**, *58* (4), 644–659. https://doi.org/10.1016/j.molcel.2015.02.033.
795 (6) Los, G. V.; Encell, L. P.; McDougall, M. G.; Hartzell, D. D.; Karassina, N.; Zimprich, C.;
796 Wood, M. G.; Learish, R.; Ohana, R. F.; Urh, M.; et al. HaloTag: A Novel Protein
797 Labeling Technology for Cell Imaging and Protein Analysis. *ACS Chem Biol* **2008**, *3* (6),
798 373–382. https://doi.org/10.1021/cb800025k.

(7) Mollwitz, B.; Brunk, E.; Schmitt, S.; Pojer, F.; Bannwarth, M.; Schiltz, M.; Rothlisberger, U.; Johnsson, K. Directed Evolution of the Suicide Protein O6-Alkylguanine-DNA Alkyltransferase for Increased Reactivity Results in an Alkylated Protein with Exceptional Stability. *Biochemistry* **2012**, *51* (5), 986–994. https://doi.org/10.1021/bi2016537.

(8) Grimm Jonathan B; English Brian P; Chen Jiji; Slaughter Joel P; Zhang Zhengjian; Revyakin Andrey; Patel Ronak; Macklin John J; Normanno Davide; Singer Robert H; et al. A General Method to Improve Fluorophores for Live-Cell and Single-Molecule Microscopy. *Nature Methods* **2015**, *12* (3), 244–250. https://doi.org/10.1038/nmeth.3256.

(9) Tokunaga Makio; Imamoto Naoko; Sakata-Sogawa Kumiko. Highly Inclined Thin Illumination Enables Clear Single-Molecule Imaging in Cells. *Nature Methods* **2008**, *5* (2), 159–161. https://doi.org/10.1038/nmeth1171.

(10) Chenouard Nicolas; Smal Ihor; de Chaumont Fabrice; Maška Martin; Sbalzarini Ivo F; Gong Yuanhao; Cardinale Janick; Carthel Craig; Coraluppi Stefano; Winter Mark; et al. Objective Comparison of Particle Tracking Methods. *Nature Methods* **2014**, *11* (3), 281–289. https://doi.org/10.1038/nmeth.2808.

(11) Speiser, A.; Müller, L.-R.; Hoess, P.; Matti, U.; Obara, C. J.; Legant, W. R.; Kreshuk, A.; Macke, J. H.; Ries, J.; Turaga, S. C. Deep Learning Enables Fast and Dense Single-Molecule Localization with High Accuracy. *Nature Methods* **2021**, *18* (9), 1082–1090. https://doi.org/10.1038/s41592-021-01236-x.

(12) Boka, A. P.; Mukherjee, A.; Mir, M. Single-Molecule Tracking Technologies for Quantifying the Dynamics of Gene Regulation in Cells, Tissue and Embryos. *Development* **2021**, *148* (18). https://doi.org/10.1242/dev.199744.

(13) Needham Sarah R.; Roberts Selene K.; Arkhipov Anton; Mysore Venkatesh P.; Tynan Christopher J.; Zanetti-Domingues Laura C.; Kim Eric T.; Losasso Valeria; Korovesis Dimitrios; Hirsch Michael; et al. EGFR Oligomerization Organizes Kinase-Active Dimers into Competent Signalling Platforms. *Nature Communications* **2016**, *7*, 13307. https://doi.org/10.1038/ncomms13307.

(14) Yasui Masato; Hiroshima Michio; Kozuka Jun; Sako Yasushi; Ueda Masahiro. Automated Single-Molecule Imaging in Living Cells. *Nature Communications* **2018**, *9* (1), 3061. https://doi.org/10.1038/s41467-018-05524-7.

(15) Nixon-Abell, J.; Obara, C. J.; Weigel, A. V.; Li, D.; Legant, W. R.; Xu, C. S.; Pasolli, H. A.; Harvey, K.; Hess, H. F.; Betzig, E.; et al. Increased Spatiotemporal Resolution Reveals Highly Dynamic Dense Tubular Matrices in the Peripheral ER. *Science* **2016**, *354* (6311), AAF3928. https://doi.org/10.1126/science.aaf3928.

(16) Hansen, A. S.; Pustova, I.; Cattoglio, C.; Tjian, R.; Darzacq, X. CTCF and Cohesin Regulate Chromatin Loop Stability with Distinct Dynamics. *Elife* **2017**, *6*. https://doi.org/10.7554/eLife.25776.

(17) Paakinaho Ville; Presman Diego M.; Ball David A.; Johnson Thomas A.; Schiltz R. Louis; Levitt Peter; Mazza Davide; Morisaki Tatsuya; Karpova Tatiana S.; Hager Gordon L. Single-Molecule Analysis of Steroid Receptor and Cofactor Action in Living Cells. *Nature Communications* **2017**, *8*, 15896. https://doi.org/10.1038/ncomms15896.

(18) Izeddin, I. Single-Molecule Tracking in Live Cells Reveals Distinct Target-Search Strategies of Transcription Factors in the Nucleus. *Elife* **2014**, *3*, 26–87. https://doi.org/10.7554/ELIFE.02230.

(19) Hansen, A. S.; Woringer, M.; Grimm, J. B.; Lavis, L. D.; Tjian, R.; Darzacq, X. Robust

Model-Based Analysis of Single-Particle Tracking Experiments with Spot-On. *Elife* **2018**, *7*. https://doi.org/10.7554/eLife.33125.

(20) Ahmad; Kumar. Steroid Hormone Receptors in Cancer Development: A Target for Cancer Therapeutics. *Cancer Lett* **2011**, *300* (1), 1–9. https://doi.org/10.1016/j.canlet.2010.09.008.

(21) Saha, S.; Dey, S.; Nath, S. Steroid Hormone Receptors: Links With Cell Cycle Machinery and Breast Cancer Progression. *Front Oncol* **2021**, *11*, 620214. https://doi.org/10.3389/fonc.2021.620214.

(22) Papageorgiou, L.; Shalzi, L.; Efthimiadou, A.; Bacopoulou, F.; Chrousos, G.; Eliopoulos, E.; Vlachakis, D. Conserved Functional Motifs of the Nuclear Receptor Superfamily as Potential Pharmacological Targets. *International Journal of Epigenetics* **2021**, *1* (2). https://doi.org/10.3892/ije.2021.3.

(23) Lu, Y.; Liu, W. Selective Estrogen Receptor Degraders (SERDs): A Promising Strategy for Estrogen Receptor Positive Endocrine-Resistant Breast Cancer. *J Med Chem* **2020**, *63* (24), 15094–15114. https://doi.org/10.1021/acs.jmedchem.0c00913.

(24) Quatrini, L.; Ugolini, S. New Insights into the Cell- and Tissue-Specificity of Glucocorticoid Actions. *Cell Mol Immunol* **2021**, *18* (2), 269–278. https://doi.org/10.1038/s41423-020-00526-2.

(25) Van Royen, M. E.; van Cappellen, W. A.; Geverts, B.; Schmidt, T.; Houtsmuller, A. B.; Schaaf, M. J. M. Androgen Receptor Complexes Probe DNA for Recognition Sequences by Short Random Interactions. *J Cell Sci* **2014**, *127* (7), 1406–1416. https://doi.org/10.1242/jcs.135228.

(26) van Royen, M. E.; van Cappellen, W. A.; de Vos, C.; Houtsmuller, A. B.; Trapman, J. Stepwise Androgen Receptor Dimerization. *J Cell Sci* **2012**, *125* (8), 1970–1979. https://doi.org/10.1242/jcs.096792.

(27) Guan; Zhou; Hafner; Blake; Chalouni; Chen; De Bruyn; Giltnane; Hartman; Heidersbach; et al. Therapeutic Ligands Antagonize Estrogen Receptor Function by Impairing Its Mobility. *Cell* **2019**, *178* (4), 949–963. https://doi.org/10.1016/j.cell.2019.06.026.

(28) Stenoien David L.; Patel Kavita; Mancini Maureen G.; Dutertre Martin; Smith Carolyn L.; O'Malley Bert W.; Mancini Michael A. FRAP Reveals That Mobility of Oestrogen Receptor-a Is Ligand- and Proteasome-Dependent. *Nature cell biology* **2001**, *3* (1), 15–23. https://doi.org/10.1038/35050515.

(29) Natwick, D. E.; Collins, S. R. Optimized ILID Membrane Anchors for Local Optogenetic Protein Recruitment. *ACS Synth Biol* **2021**, *10* (5), 1009–1023. https://doi.org/10.1021/acssynbio.0c00511.

(30) Heckert, A.; Dahal, L.; Tjian, R.; Darzacq, X. Recovering Mixtures of Fast-Diffusing States from Short Single-Particle Trajectories. *Elife* **2022**, *11*. https://doi.org/10.7554/eLife.70169.

(31) Zhang, J.-H.; Chung, T. D. Y.; Oldenburg, K. R. A Simple Statistical Parameter for Use in Evaluation and Validation of High Throughput Screening Assays. *J Biomol Screen* **1999**, *4* (2), 67–73. https://doi.org/10.1177/108705719900400206.

(32) Kuiper, G. G. J. M.; Carlsson, B.; Grandien, K.; Enmark, E.; Häggblad, J.; Nilsson, S.; Gustafsson, J.-Å. Comparison of the Ligand Binding Specificity and Transcript Tissue Distribution of Estrogen Receptors α and β. *Endocrinology* **1997**, *138* (3), 863–870. https://doi.org/10.1210/endo.138.3.4979.

(33) Liu, Z.; Legant, W. R.; Chen, B.-C.; Li, L.; Grimm, J. B.; Lavis, L. D.; Betzig, E.; Tjian, R. 3D Imaging of Sox2 Enhancer Clusters in Embryonic Stem Cells. *Elife* **2014**, *3*, E4236. https://doi.org/10.7554/eLife.04236.

(34) Mazza, D.; Abernathy, A.; Golob, N.; Morisaki, T.; McNally, J. G. A Benchmark for Chromatin Binding Measurements in Live Cells. *Nucleic Acids Res* **2012**, *40* (15), E119. https://doi.org/10.1093/nar/gks701.

(35) Elf, J.; Li, G.-W.; Xie, X. S. Probing Transcription Factor Dynamics at the Single-Molecule Level in a Living Cell. *Science* **2007**, *316* (5828), 1191–1194. https://doi.org/10.1126/science.1141967.

(36) Chen, Y.-C.; Yu, J.; Metcalfe, C.; De Bruyn, T.; Gelzleichter, T.; Malhi, V.; Perez-Moreno, P. D.; Wang, X. Latest Generation Estrogen Receptor Degraders for the Treatment of Hormone Receptor-Positive Breast Cancer. *Expert Opin Investig Drugs* **2022**, *31* (6), 515–529. https://doi.org/10.1080/13543784.2021.1983542.

(37) Kahraman, M.; Govek, S. P.; Nagasawa, J. Y.; Lai, A.; Bonnefous, C.; Douglas, K.; Sensintaffar, J.; Liu, N.; Lee, K.; Aparicio, A.; et al. Maximizing ER-α Degradation Maximizes Activity in a Tamoxifen-Resistant Breast Cancer Model: Identification of GDC-0927. *ACS Med Chem Lett* **2019**, *10* (1), 50–55. https://doi.org/10.1021/acsmedchemlett.8b00414.

(38) Wells, C. I.; Vasta, J. D.; Corona, C. R.; Wilkinson, J.; Zimprich, C. A.; Ingold, M. R.; Pickett, J. E.; Drewry, D. H.; Pugh, K. M.; Schwinn, M. K.; et al. Quantifying CDK Inhibitor Selectivity in Live Cells. *Nature Communications* **2020**, *11* (1). https://doi.org/10.1038/s41467-020-16559-0.

(39) Wang; Wu; Wu; Chen; Zou; Wang; Wu; Hu; Jiang; Liu; et al. Discovery of 4-(((4-(5-Chloro-2-(((1s,4s)-4-((2-Methoxyethyl)Amino)Cyclohexyl)Amino)Pyridin-4-Yl)Thiazol-2-Yl)Amino)Methyl)Tetrahydro-2H-Pyran-4-Carbonitrile (JSH-150) as a Novel Highly Selective and Potent CDK9 Kinase Inhibitor. *Eur J Med Chem* **2018**, *158*, 896–916. https://doi.org/10.1016/j.ejmech.2018.09.025.

(40) Olson Calla M; Jiang Baishan; Erb Michael A; Liang Yanke; Doctor Zainab M; Zhang Zinan; Zhang Tinghu; Kwiatkowski Nicholas; Boukhali Myriam; Green Jennifer L; et al. Pharmacological Perturbation of CDK9 Using Selective CDK9 Inhibition or Degradation. *Nature Chemical Biology* **2018**, *14* (2), 163–170. https://doi.org/10.1038/nchembio.2538.

(41) Parry, D.; Guzi, T.; Shanahan, F.; Davis, N.; Prabhavalkar, D.; Wiswell, D.; Seghezzi, W.; Paruch, K.; Dwyer, M. P.; Doll, R.; et al. Dinaciclib (SCH 727965), a Novel and Potent Cyclin-Dependent Kinase Inhibitor. *Mol Cancer Ther* **2010**, *9* (8), 2344–2353. https://doi.org/10.1158/1535-7163.MCT-10-0324.

(42) Menezes, D. L.; Taverna, P.; Jensen, M. R.; Abrams, T.; Stuart, D.; Yu, G. K.; Duhl, D.; Machajewski, T.; Sellers, W. R.; Pryer, N. K.; et al. The Novel Oral Hsp90 Inhibitor NVP-HSP990 Exhibits Potent and Broad-Spectrum Antitumor Activities In Vitro and In Vivo. *Mol Cancer Ther* **2012**, *11* (3), 730–739. https://doi.org/10.1158/1535-7163.MCT-11-0667.

(43) McCleese, J. K.; Bear, M. D.; Fossey, S. L.; Mihalek, R. M.; Foley, K. P.; Ying, W.; Barsoum, J.; London, C. A. The Novel HSP90 Inhibitor STA-1474 Exhibits Biologic Activity against Osteosarcoma Cell Lines. *Int J Cancer* **2009**, *125* (12), 2792–2801. https://doi.org/10.1002/ijc.24660.

(44) Bussenius, J.; Blazey, C. M.; Aay, N.; Anand, N. K.; Arcalas, A.; Baik, T.; Bowles, O. J.; Buhr, C. A.; Costanzo, S.; Curtis, J. K.; et al. Discovery of XL888: A Novel Tropane-

Derived Small Molecule Inhibitor of HSP90. *Bioorg Med Chem Lett* **2012**, *22* (17), 5396–5404. https://doi.org/10.1016/j.bmcl.2012.07.052.

(45) Apsel Beth; Blair Jimmy A; Gonzalez Beatriz; Nazif Tamim M; Feldman Morri E; Aizenstein Brian; Hoffman Randy; Williams Roger L; Shokat Kevan M; Knight Zachary A. Targeted Polypharmacology: Discovery of Dual Inhibitors of Tyrosine and Phosphoinositide Kinases. *Nature Chemical Biology* **2008**, *4* (11), 691–699. https://doi.org/10.1038/nchembio.117.

(46) Thoreen, C. An ATP-Competitive Mammalian Target of Rapamycin Inhibitor Reveals Rapamycin-Resistant Functions of MTORC1. *J Biol Chem* **2009**, *284* (12), 8020–8029. https://doi.org/10.1074/JBC.M900301200.

(47) Yu, K.; Toral-Barza, L.; Shi, C.; Zhang, W.-G.; Lucas, J.; Shor, B.; Kim, J.; Verheijen, J.; Curran, K.; Malwitz, D. J.; et al. Biochemical, Cellular, and In Vivo Activity of Novel ATP-Competitive and Selective Inhibitors of the Mammalian Target of Rapamycin. *Cancer Res* **2009**, *69* (15), 6232–6240. https://doi.org/10.1158/0008-5472.CAN-09-0299.

(48) Adams, J.; Palombella, V. J.; Sausville, E. A.; Johnson, J.; Destree, A.; Lazarus, D. D.; Maas, J.; Pien, C. S.; Prakash, S.; Elliott, P. J. Proteasome Inhibitors: A Novel Class of Potent and Effective Antitumor Agents. *Cancer Res* **1999**, *59* (11), 2615–2622.

(49) Kuhn; Chen; Voorhees; Strader; Shenk; Sun; Demo; Bennett; van Leeuwen; Chanan-Khan; et al. Potent Activity of Carfilzomib, a Novel, Irreversible Inhibitor of the Ubiquitin-Proteasome Pathway, against Preclinical Models of Multiple Myeloma. *Blood* **2007**, *110* (9), 3281–3290. https://doi.org/10.1182/blood-2007-01-065888.

(50) Mroczkiewicz, M.; Winkler, K.; Nowis, D.; Placha, G.; Golab, J.; Ostaszewski, R. Studies of the Synthesis of All Stereoisomers of MG-132 Proteasome Inhibitors in the Tumor Targeting Approach. *J Med Chem* **2010**, *53* (4), 1509–1518. https://doi.org/10.1021/jm901619n.

(51) Franco, L. C.; Morales, F.; Boffo, S.; Giordano, A. CDK9: A Key Player in Cancer and Other Diseases. *J Cell Biochem* **2017**, *119* (2), 1273–1284. https://doi.org/10.1002/jcb.26293.

(52) Shah, Y. M.; Rowan, B. G. The Src Kinase Pathway Promotes Tamoxifen Agonist Action in Ishikawa Endometrial Cells through Phosphorylation-Dependent Stabilization of Estrogen Receptor Promoter Interaction and Elevated Steroid Receptor Coactivator 1 Activity. *Mol Endocrinol* **2005**, *19* (3), 732–748. https://doi.org/10.1210/ME.2004-0298.

(53) Anbalagan; Rowan. Estrogen Receptor Alpha Phosphorylation and Its Functional Impact in Human Breast Cancer. *Mol Cell Endocrinol* **2015**, *418*, 264–272. https://doi.org/10.1016/j.mce.2015.01.016.

(54) Liang, J.; Zbieg, J. R.; Blake, R. A.; Chang, J. H.; Daly, S.; DiPasquale, A. G.; Friedman, L. S.; Gelzleichter, T.; Gill, M.; Giltnane, J. M.; et al. GDC-9545 (Giredestrant): A Potent and Orally Bioavailable Selective Estrogen Receptor Antagonist and Degrader with an Exceptional Preclinical Profile for ER+ Breast Cancer. *J Med Chem* **2021**, *64* (16), 11841–11856. https://doi.org/10.1021/acs.jmedchem.1c00847.

(55) Wardell, S. E.; Ellis, M. J.; Alley, H. M.; Eisele, K.; VanArsdale, T.; Dann, S. G.; Arndt, K. T.; Primeau, T.; Griffin, E.; Shao, J.; et al. Efficacy of SERD/SERM Hybrid-CDK4/6 Inhibitor Combinations in Models of Endocrine Therapy–Resistant Breast Cancer. *Clin Cancer Res* **2015**, *21* (22), 5121–5130. https://doi.org/10.1158/1078-0432.CCR-15-0360.

(56) Finn, R. S.; Aleshin, A.; Slamon, D. J. Targeting the Cyclin-Dependent Kinases (CDK) 4/6 in Estrogen Receptor-Positive Breast Cancers. *Breast Cancer Research* **2016**, *18* (1).

https://doi.org/10.1186/s13058-015-0661-5.
(57) Mueller, F.; Stasevich, T. J.; Mazza, D.; McNally, J. G. Quantifying Transcription Factor Kinetics: At Work or at Play? *Critical Reviews in Biochemistry and Molecular Biology* **2013**, *48* (5), 492–514. https://doi.org/10.3109/10409238.2013.833891.
(58) Chu, Q.; Wang, J.; Du, Y.; Zhou, T.; Shi, A.; Xiong, J.; Ji, W.-K.; Deng, L. Oligomeric CHMP7 Mediates Three-Way ER Junctions and ER-Mitochondria Interactions. *Cell Death and Differentiation* **2022**, 1–17. https://doi.org/10.1038/s41418-022-01048-2.
(59) Sergé Arnauld; Bertaux Nicolas; Rigneault Hervé; Marguet Didier. Dynamic Multiple-Target Tracing to Probe Spatiotemporal Cartography of Cell Membranes. *Nature Methods* **2008**, *5* (8), 687–694. https://doi.org/10.1038/nmeth.1233.
(60) Levenberg, K. A Method for the Solution of Certain Non-Linear Problems in Least Squares. *Quarterly of applied mathematics* **1944**, *2* (2), 164–168. https://doi.org/10.1090/qam/10666.
(61) Donald W. Marquardt. An Algorithm for Least-Squares Estimation of Nonlinear Parameters. *Journal of the Society for Industrial and Applied Mathematics* **1963**, *11* (2), 431–441. https://doi.org/10.1137/0111030.
(62) Laurence Ted A; Chromy Brett A. Efficient Maximum Likelihood Estimator Fitting of Histograms. *Nature Methods* **2010**, *7* (5), 338–339. https://doi.org/10.1038/nmeth0510-338.
(63) Smith Carlas S; Joseph Nikolai; Rieger Bernd; Lidke Keith A. Fast, Single-Molecule Localization That Achieves Theoretically Minimum Uncertainty. *Nature Methods* **2010**, No. 5, 373–375. https://doi.org/10.1038/nmeth.1449.
(64) Parthasarathy Raghuveer. Rapid, Accurate Particle Tracking by Calculation of Radial Symmetry Centers. *Nature Methods* **2012**, *9* (7), 724–726. https://doi.org/10.1038/nmeth.2071.
(65) Sbalzarini, I. F.; Koumoutsakos, P. Feature Point Tracking and Trajectory Analysis for Video Imaging in Cell Biology. *J Struct Biol* **2005**, *151* (2), 182–195. https://doi.org/10.1016/j.jsb.2005.06.002.
(66) Olaf Ronneberger; Philipp Fischer; Thomas Brox. U-Net: Convolutional Networks for Biomedical Image Segmentation. In *Medical Image Computing and Computer-Assisted Intervention – MICCAI 2015*; Springer International Publishing, 2015; pp 234–241. https://doi.org/10.1007/978-3-319-24574-4_28.
(67) Bemis, G. W.; Murcko, M. A. The Properties of Known Drugs. 1. Molecular Frameworks. *J Med Chem* **1996**, *39* (15), 2887–2893. https://doi.org/10.1021/jm9602928.
(68) Stirling, D. R.; Swain-Bowden, M. J.; Lucas, A. M.; Carpenter, A. E.; Cimini, B. A.; Goodman, A. CellProfiler 4: Improvements in Speed, Utility and Usability. *BMC Bioinformatics* **2021**, *22* (1). https://doi.org/10.1186/s12859-021-04344-9.

Figure 1

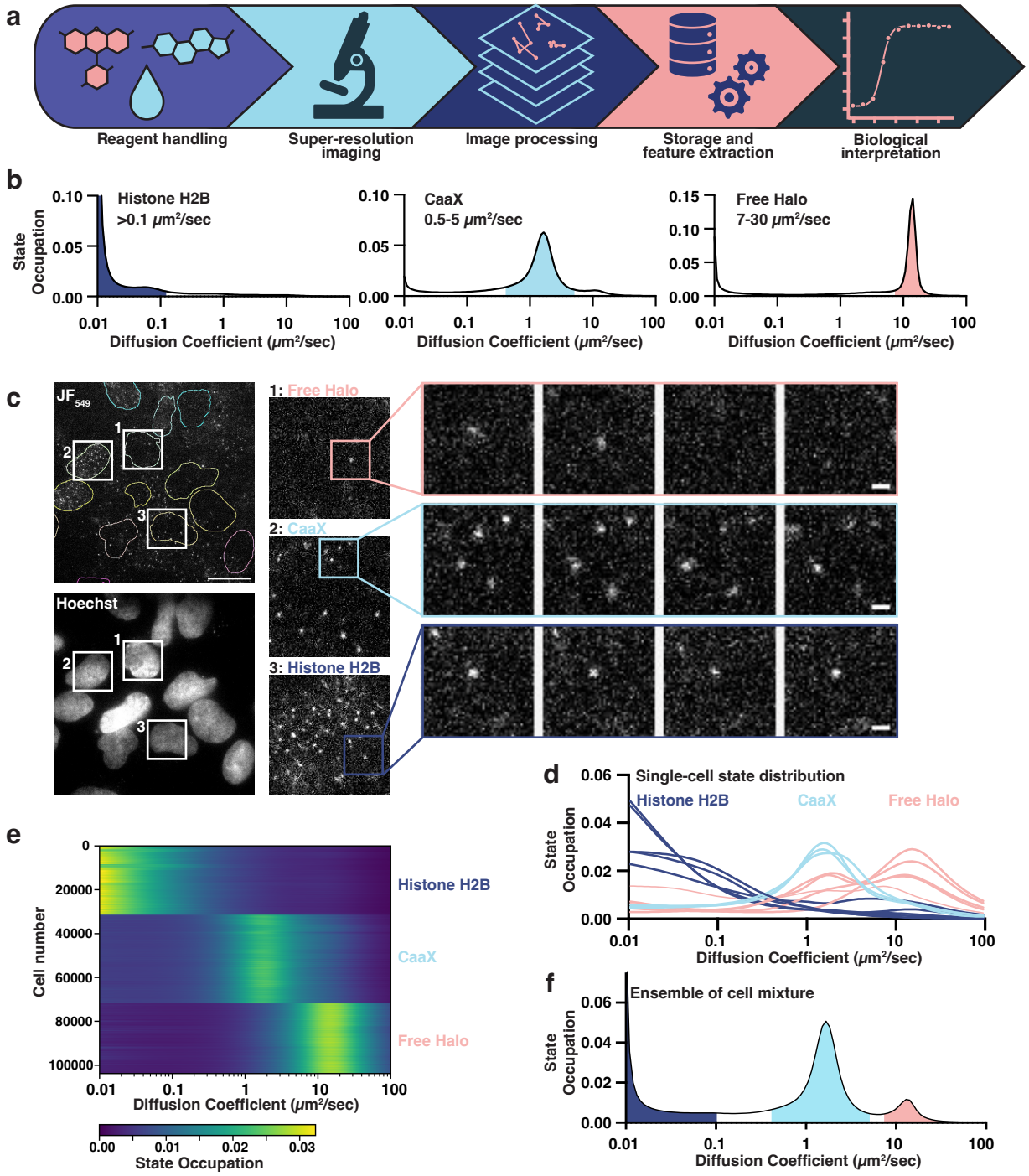
a
Reagent handling
Super-resolution imaging
Image processing
Storage and feature extraction
Biological interpretation
b
Histone H2B
>0.1 μm²/sec
CaaX
0.5-5 μm²/sec
Free Halo
7-30 μm²/sec
State Occupation
Diffusion Coefficient (μm²/sec)
c
JF549
Hoechst
1: Free Halo
2: CaaX
3: Histone H2B
d
Single-cell state distribution
Histone H2B
CaaX
Free Halo
State Occupation
Diffusion Coefficient (μm²/sec)
e
Cell number
Histone H2B
CaaX
Free Halo
Diffusion Coefficient (μm²/sec)
State Occupation
f
Ensemble of cell mixture
State Occupation
Diffusion Coefficient (μm²/sec)

Figure 2

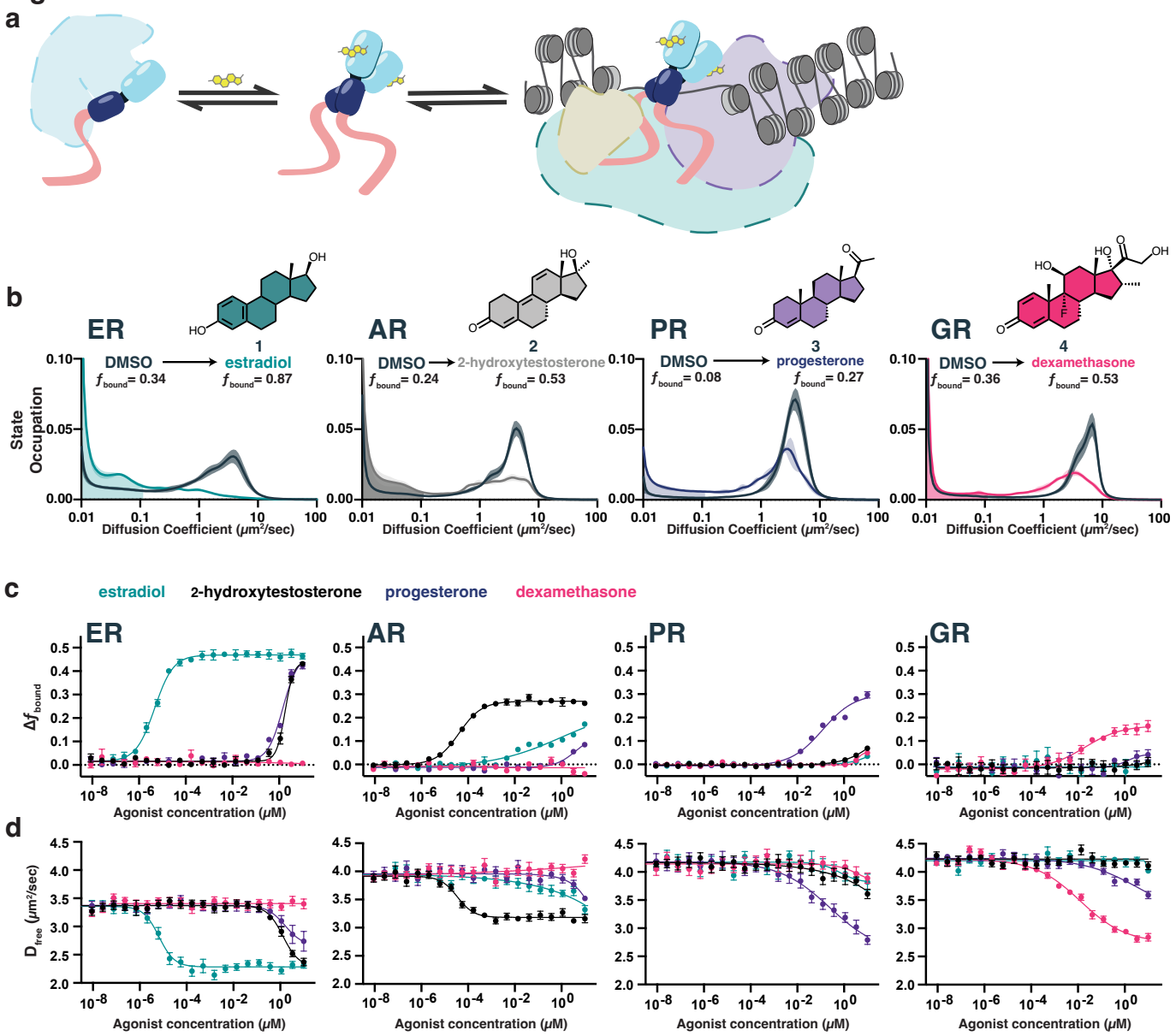
a
b
ER
AR
PR
GR
1
2
3
4
DMSO → estradiol
f_{bound}= 0.34
f_{bound}= 0.87
DMSO → 2-hydroxytestosterone
f_{bound}= 0.24
f_{bound}= 0.53
DMSO → progesterone
f_{bound}= 0.08
f_{bound}= 0.27
DMSO → dexamethasone
f_{bound}= 0.36
f_{bound}= 0.53
State Occupation
Diffusion Coefficient (μm²/sec)
c
estradiol
2-hydroxytestosterone
progesterone
dexamethasone
Δf_{bound}
Agonist concentration (μM)
d
D_{free} (μm²/sec)
Agonist concentration (μM)

Figure 3

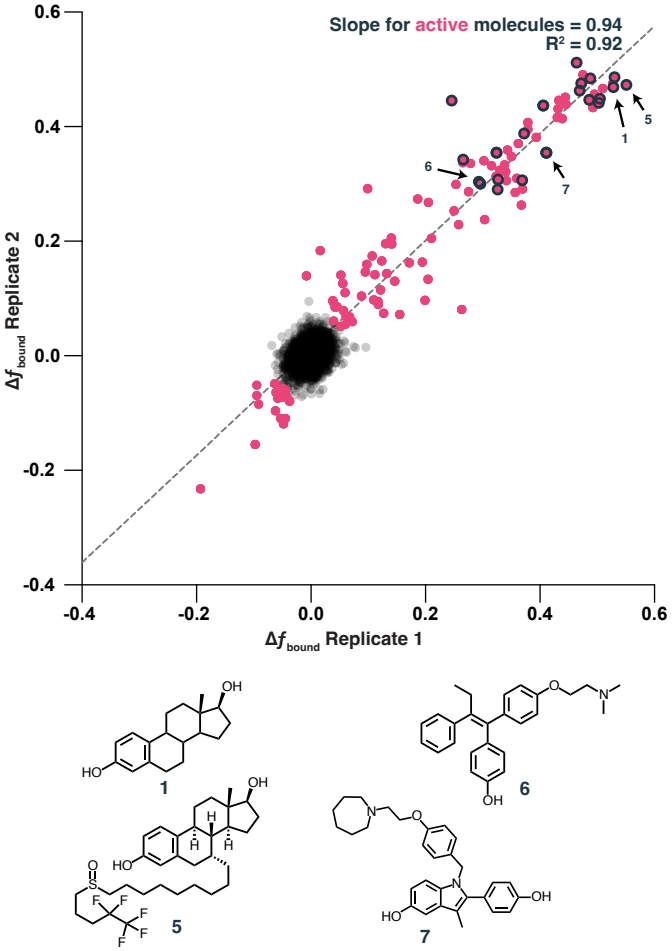
Slope for active molecules = 0.94
R² = 0.92
0.6
0.4
0.2
0.0
-0.2
-0.4
-0.4
-0.2
0.0
0.2
0.4
0.6
Δf bound Replicate 2
Δf bound Replicate 1
1
5
6
7
OH
HO
H
O
S
F
N
1
5
6
7

Figure 4

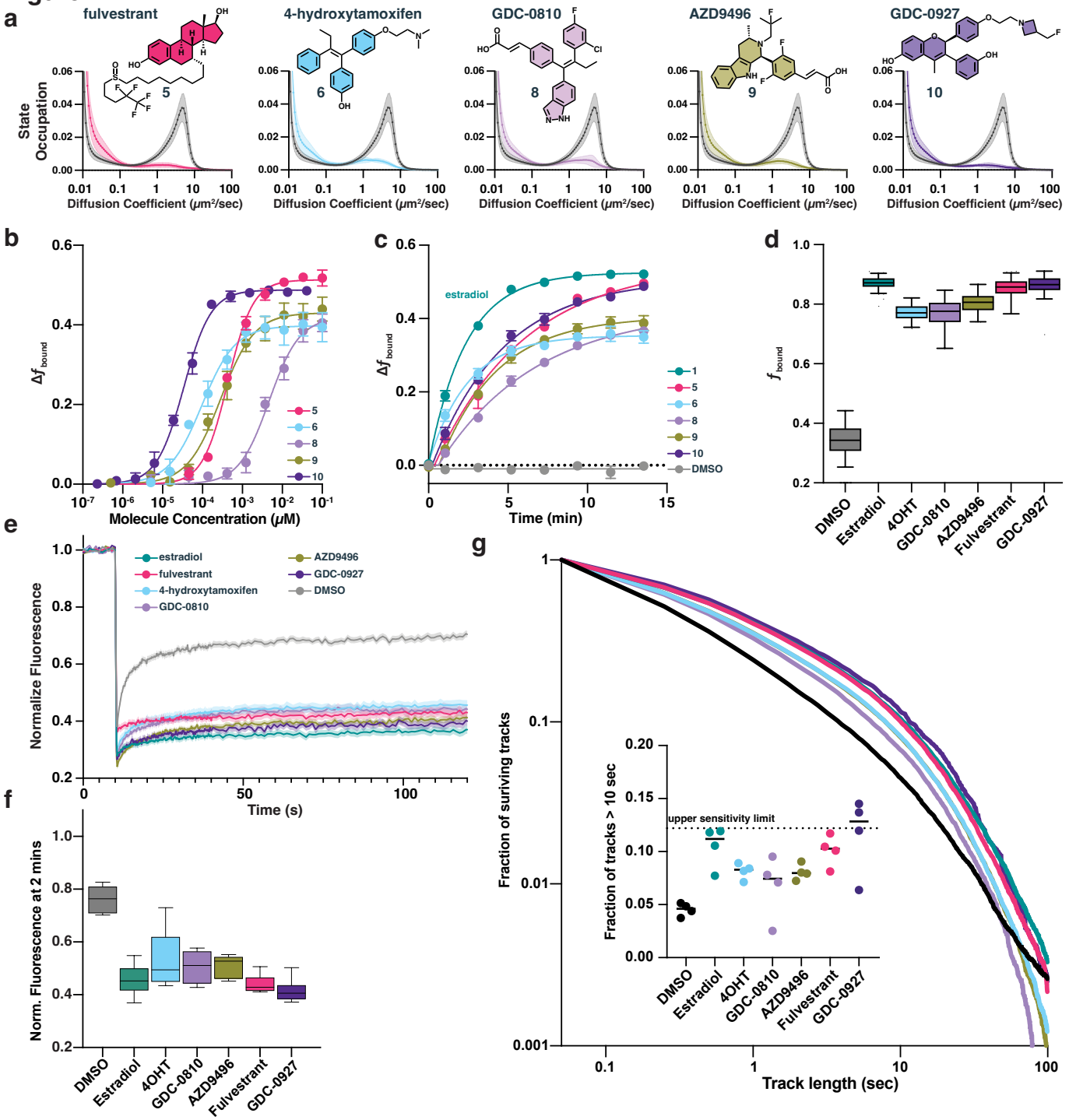
a
fulvestrant
4-hydroxytamoxifen
GDC-0810
AZD9496
GDC-0927
State Occupation
Diffusion Coefficient (μm²/sec)
b
Molecule Concentration (μM)
c
estradiol
Time (min)
d
DMSO
Estradiol
4OHT
GDC-0810
AZD9496
Fulvestrant
GDC-0927
e
Normalize Fluorescence
Time (s)
f
Norm. Fluorescence at 2 mins
g
Fraction of suriving tracks
Track length (sec)
Fraction of tracks > 10 sec
upper sensitivity limit

Figure 5

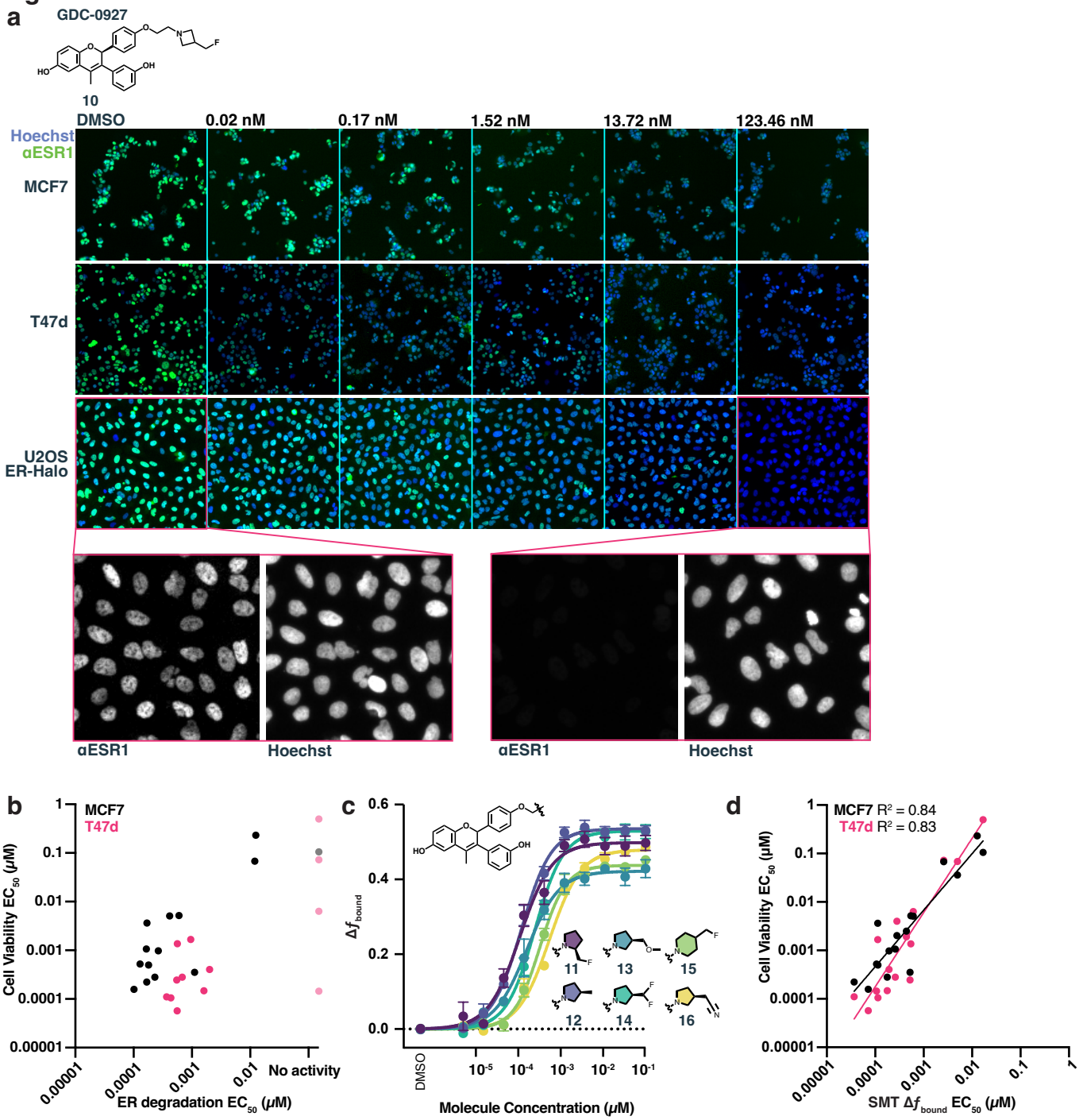
a
GDC-0927
10
DMSO
0.02 nM
0.17 nM
1.52 nM
13.72 nM
123.46 nM
Hoechst
αESR1
MCF7
T47d
U2OS
ER-Halo
αESR1
Hoechst
αESR1
Hoechst
b
MCF7
T47d
Cell Viability EC50 (μM)
ER degradation EC50 (μM)
No activity
c
Δf bound
DMSO
Molecule Concentration (μM)
11
12
13
14
15
16
d
MCF7 R² = 0.84
T47d R² = 0.83
Cell Viability EC50 (μM)
SMT Δf bound EC50 (μM)

Figure 6

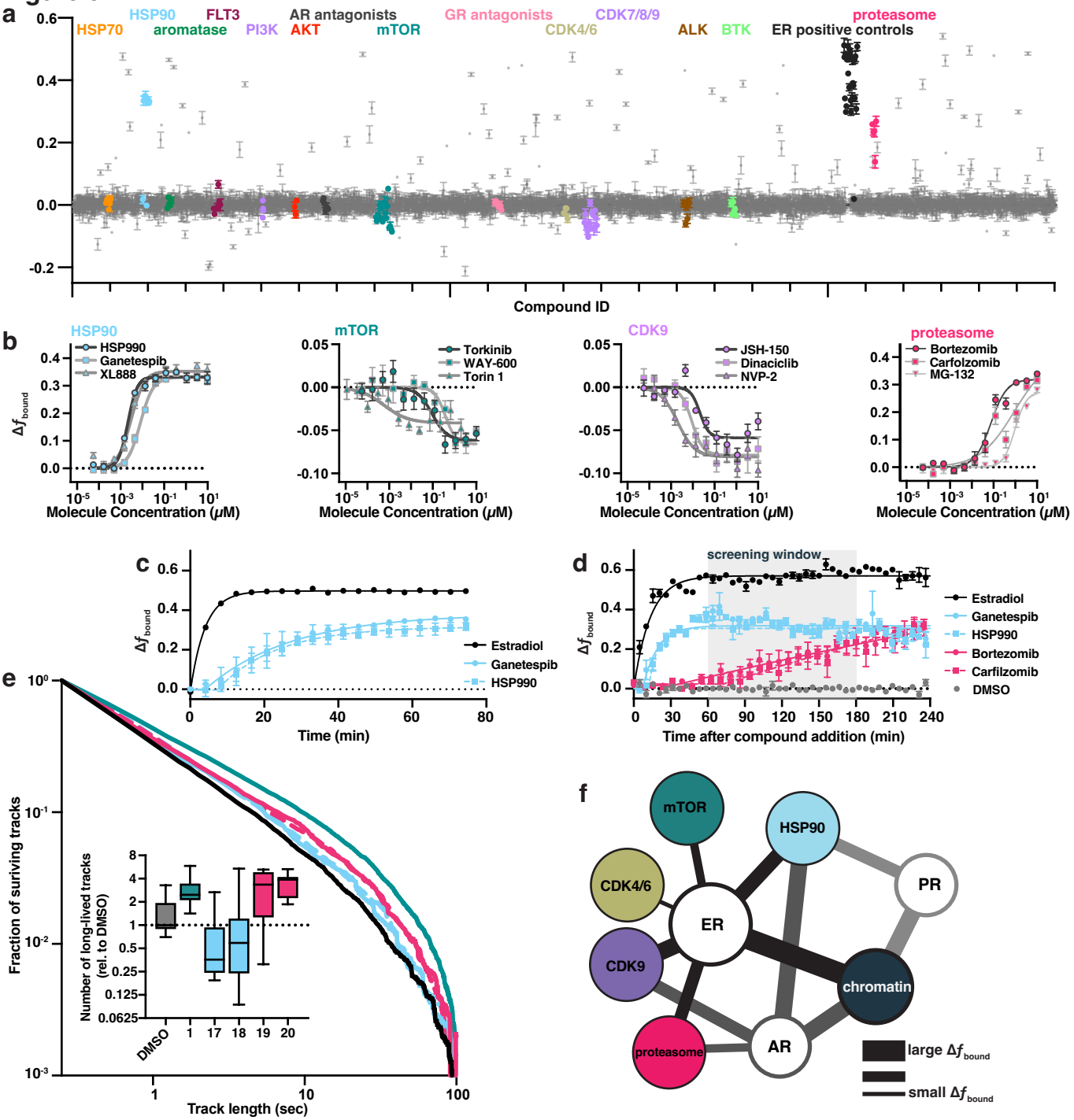
a
HSP70
HSP90
aromatase
FLT3
PI3K
AR antagonists
AKT
mTOR
GR antagonists
CDK4/6
CDK7/8/9
ALK
BTK
ER positive controls
proteasome
Compound ID
b
HSP90
HSP990
Ganetespib
XL888
mTOR
Torkinib
WAY-600
Torin 1
CDK9
JSH-150
Dinaciclib
NVP-2
proteasome
Bortezomib
Carfolzomib
MG-132
Molecule Concentration (μM)
c
Estradiol
Ganetespib
HSP990
Time (min)
d
screening window
Estradiol
Ganetespib
HSP990
Bortezomib
Carfilzomib
DMSO
Time after compound addition (min)
e
Fraction of suriving tracks
Track length (sec)
Number of long-lived tracks (rel. to DMSO)
DMSO
f
mTOR
HSP90
CDK4/6
PR
ER
CDK9
chromatin
proteasome
AR
large Δf bound
small Δf bound

Extended Data 1

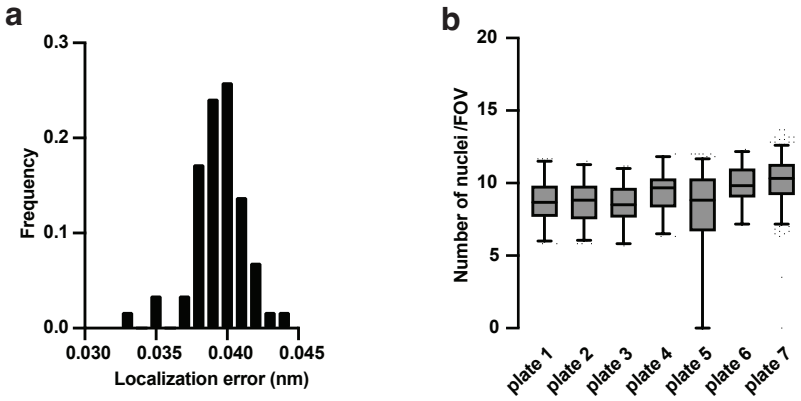

Extended data 2

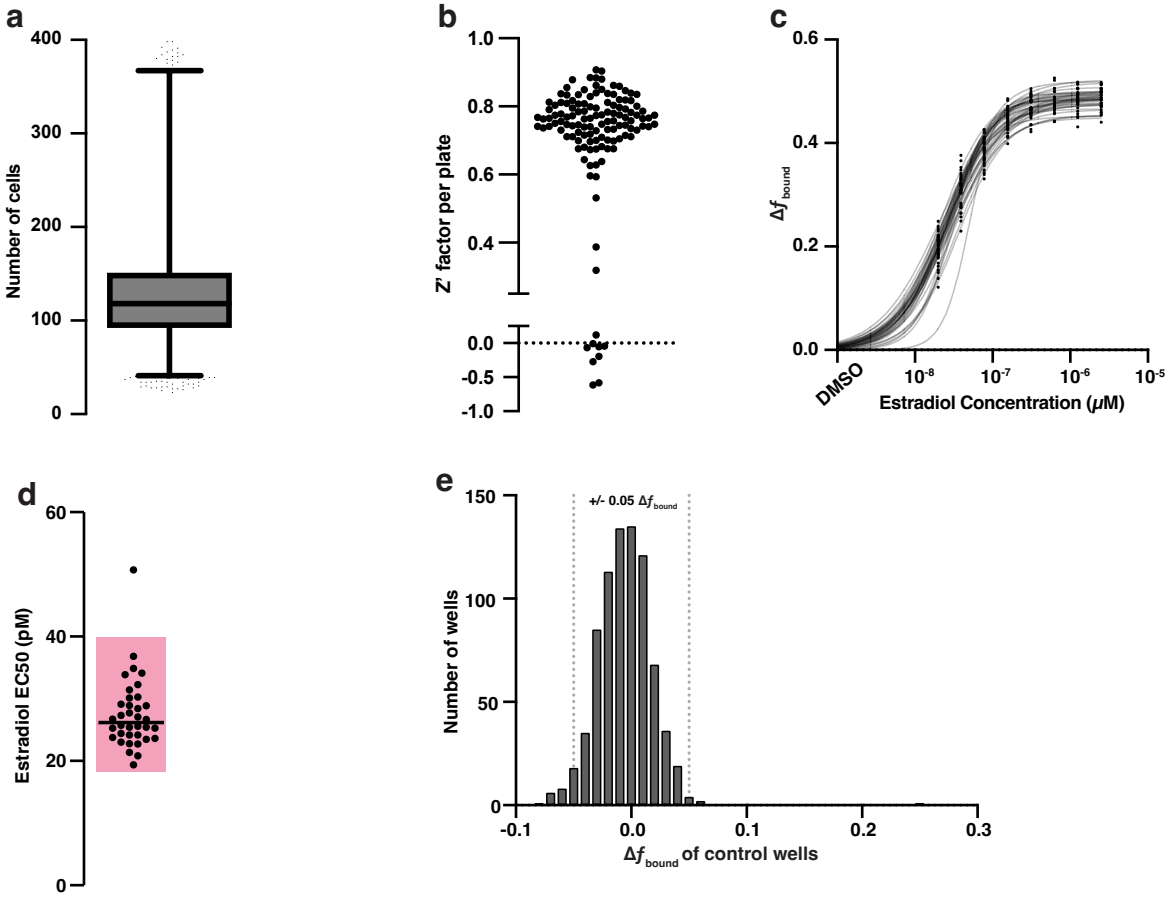

Extended data 3

a

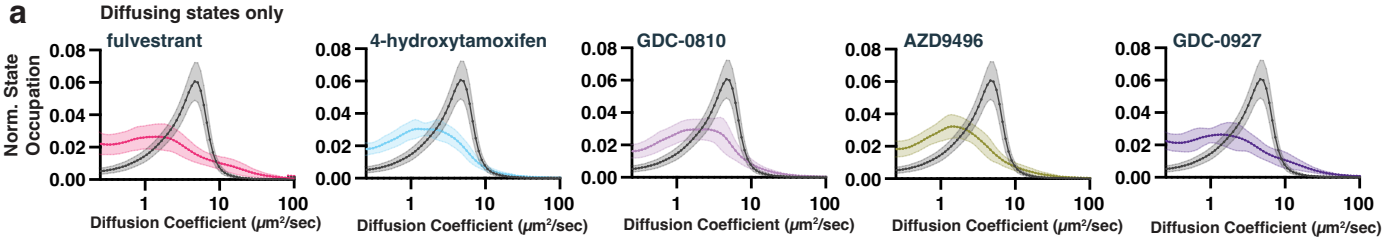

b

Compound	X_o (min)	$T_{1/2}$ (min)	E_{Max}
Estradiol	0	1.6	0.53
Fulvestrant	0.3	3.9	0.55
Tamoxifen	0	1.7	0.35
GDC-0810	0.6	4.3	0.43
GDC-0927	0.2	3.1	0.51
AZD9496	0.6	2.5	0.41

c

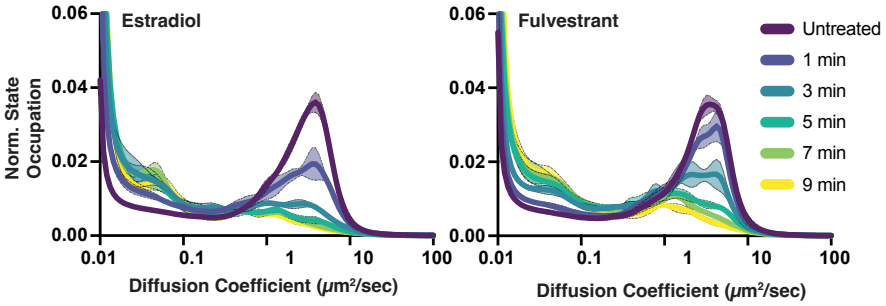

d

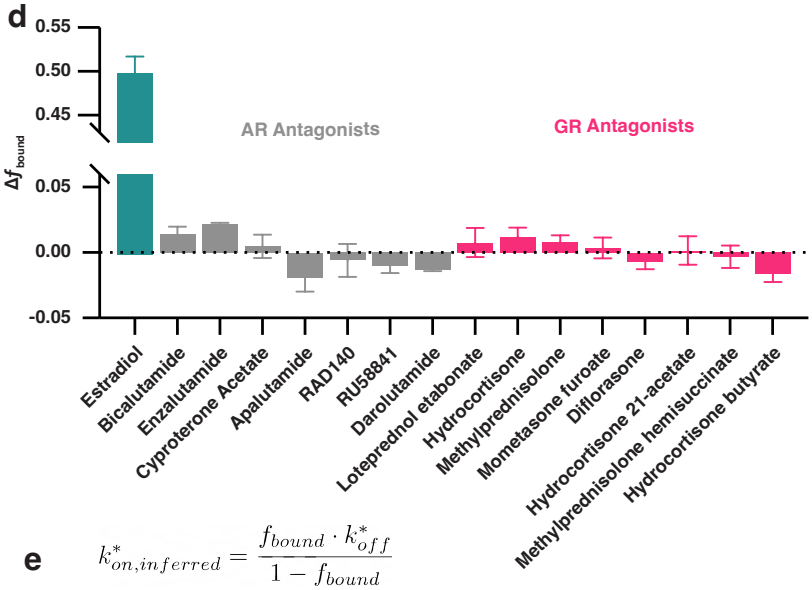

e

$$k^*_{on,inferred} = \frac{f_{bound} \cdot k^*_{off}}{1 - f_{bound}}$$

Compound	k_{slow} (s^{-1})	Rel. to DMSO	f_{bound}	$k_{on,\ inferred}$
DMSO	0.17	1	0.34	0.08
Estradiol	0.11*	1.60	0.87	*0.73**
Fulvestrant	0.11*	1.55	0.85	*0.62**
Tamoxifen	0.12	1.38	0.77	0.40
GDC-0810	0.14	1.27	0.78	0.50
GDC-0927	0.09*	1.82	0.87	*0.60**
AZD9496	0.12	1.39	0.88	0.88

Extended Data 4

a

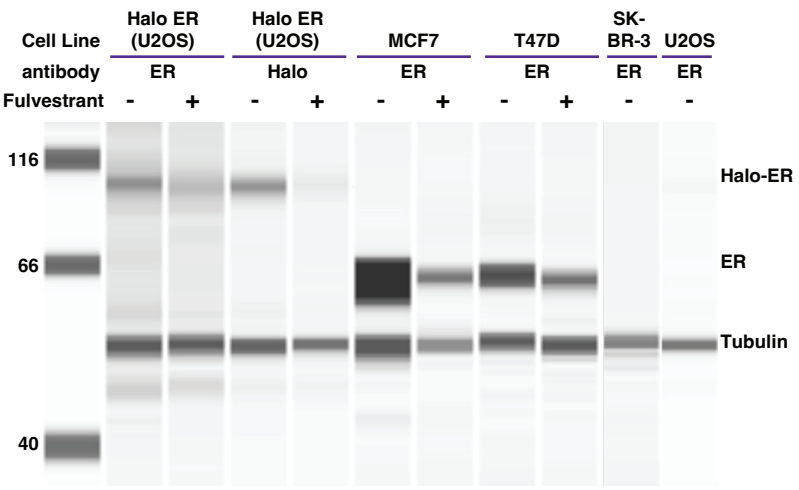

b

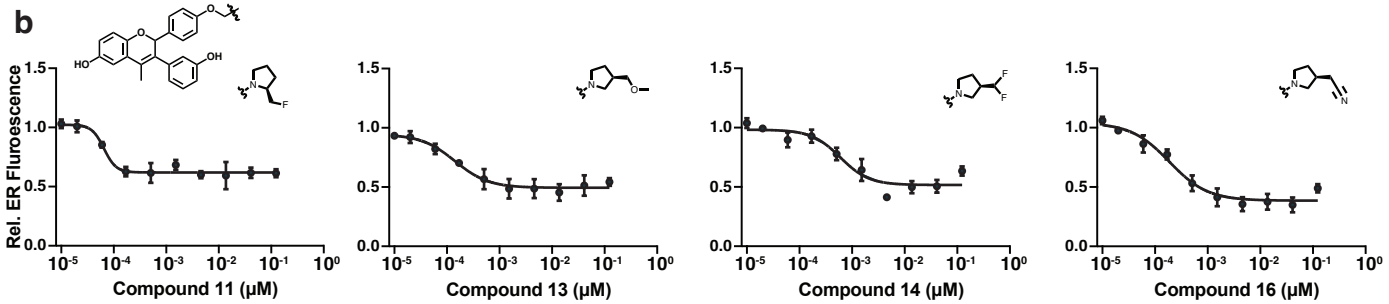

c

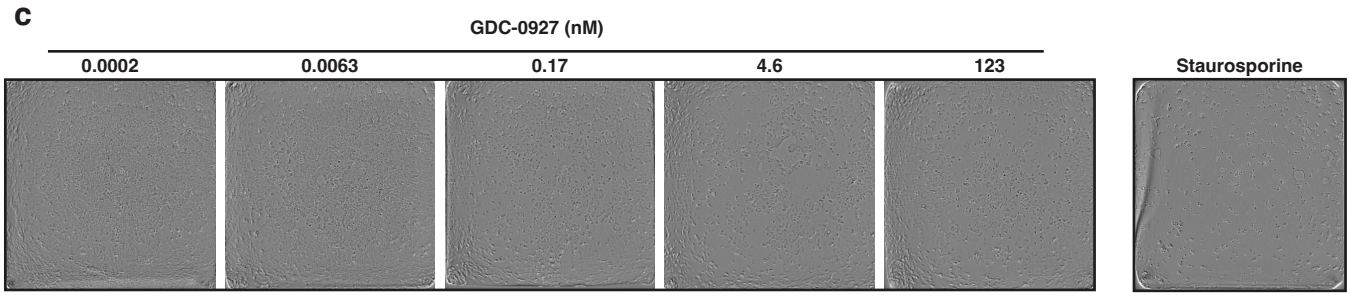

d

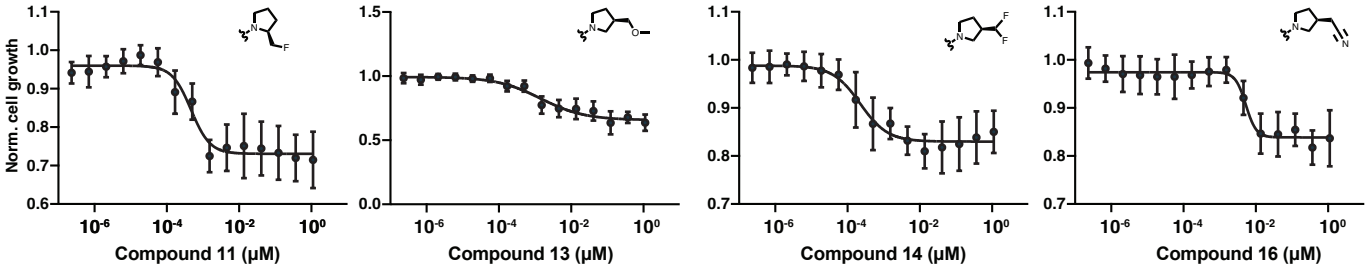

Extended Data 5

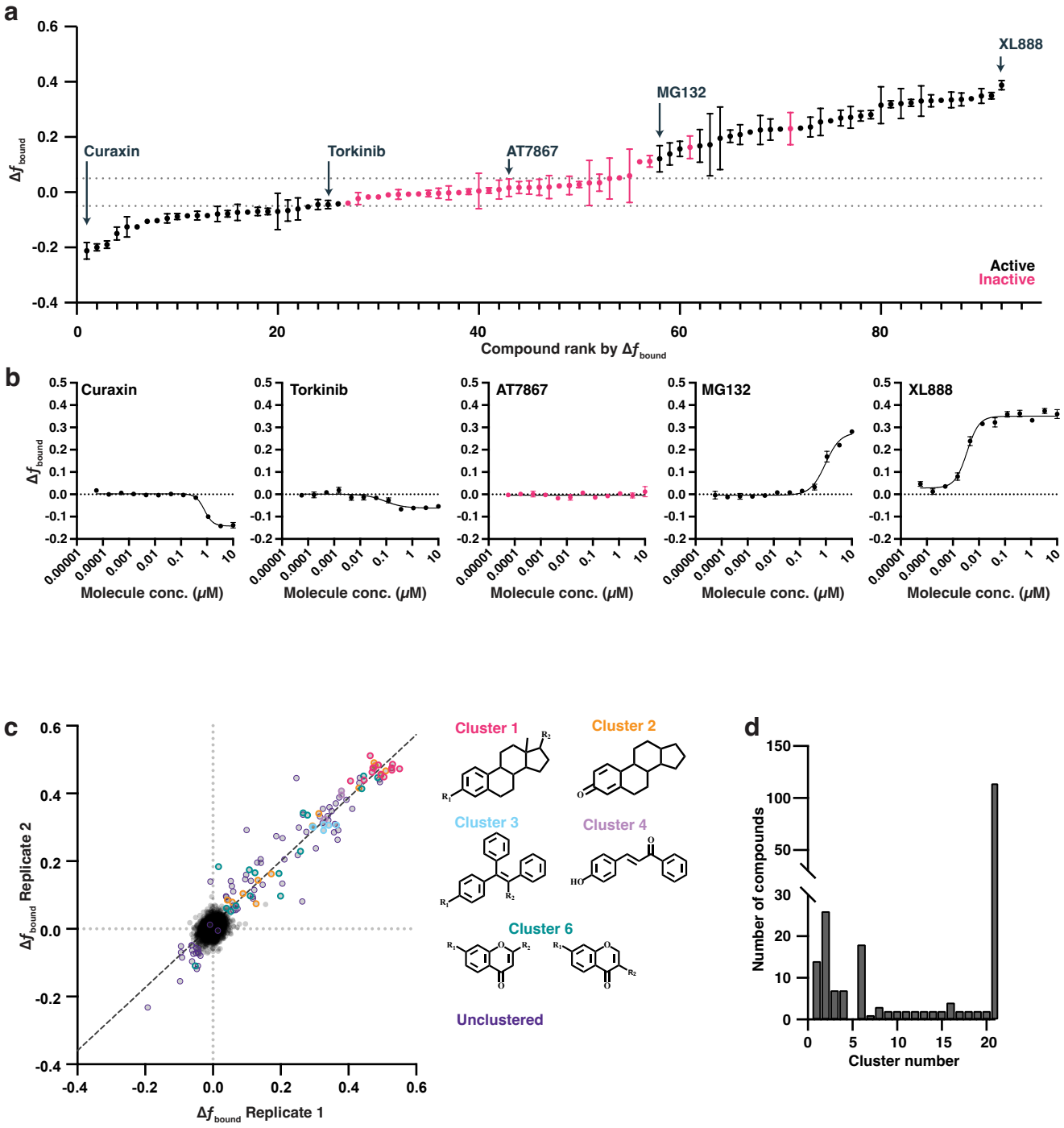

Extended Data 6

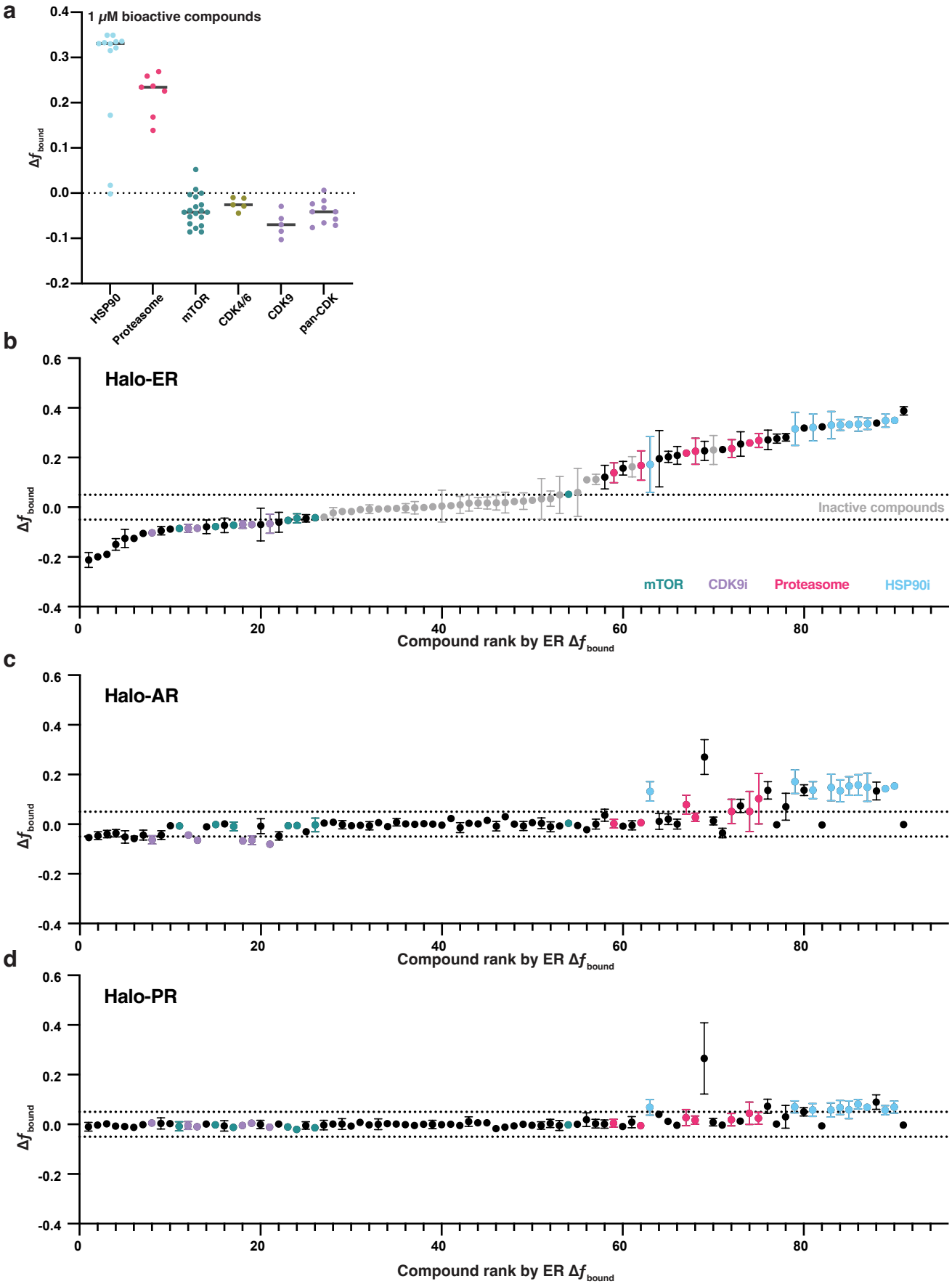
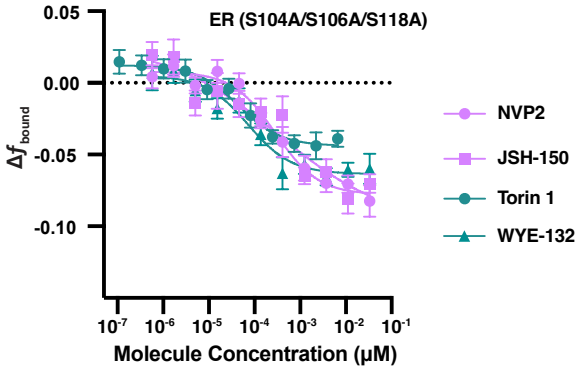
Extended Data 7